Metabotropic signaling within somatostatin interneurons regulates thalamocortical inputs during development

Deepanjali Dwivedi[1,2], Dimitri Dumontier[3], Mia Sherer[1,2], Sherry Lin[1], Andrea MC Mirow[1,2,3], Yanjie Qiu[1,2], Qing Xu[1,2,4], Samuel A. Liebman[3], Djeckby Joseph[3], Sandeep R Datta[1], Gord Fishell[1,2,*], Gabrielle Pouchelon[1,2,3*].

[1] Harvard Medical School, Department of Neurobiology, Boston, Massachusetts, USA.
[2] Broad Institute, Stanley Center for Psychiatric Research, Cambridge, Massachusetts, USA.
[3] Cold Spring Harbor Laboratory, Cold Spring Harbor, NY, USA
[4] Center for Genomics & Systems Biology, New York University Abu Dhabi, Abu Dhabi, UAE

* Corresponding authors: G.P. (pouchel@cshl.edu); G.F. (gordon_fishell@hms.harvard.edu)
Lead contact: G.P. (pouchel@cshl.edu)

Summary

During brain development, neural circuits undergo major activity-dependent restructuring. In contrast to other cortical neurons, somatostatin interneurons primarily receive strong thalamocortical inputs, which regress as the animals mature. Yet, the mechanisms underlying such transient connectivity are unknown. In contrast to other known connectivity, we found that transient thalamocortical inputs onto somatostatin interneurons is inversely correlated with postsynaptic neuron activity. Transient inputs recruit metabotropic mediated transcription supporting the later elimination of this connectivity, known to regulate the development of cortical networks. In particular, cell-type specific metabotropic glutamatergic receptor 1 regulates transcriptional levels of the guidance molecule, semaphorin 3A. Remarkably, we found that this developmental process impacts the development of normal exploratory behavior of adult mice. Synaptic maturation is usually thought to be activity-dependent and largely controlled presynaptically. However, our results indicate that thalamocortical afferents are regulated by negative metabotropic feedback from postsynaptic somatostatin cells and that this mechanism underlies the maturation of proper adult circuit functions.

Introduction

Bottom-up afferents from the thalamus provide topographical precise sensory inputs to the neocortex. These sensory inputs target both excitatory and inhibitory cortical neuron populations and undergo dramatic refinement during development. It is well accepted that both genetic and activity-dependent factors are required for appropriate circuit development, but at present it is unclear how these factors interact to recalibrate thalamocortical (TC) circuits for adult function.[1–3]

In the adult somatosensory cortex, feedforward inhibition (FFI) from TC inputs onto excitatory neurons and parvalbumin (PV) inhibitory cortical interneurons (cINs), as well as feedback inhibition from excitatory neurons to somatostatin (SST) cINs play a crucial role in regulating adult circuit function.[4–6] The developmental pattern of connectivity expressed by TC afferents with their neuron targets (the FFI) supports the broad principle that weak connections are strengthened over time during circuit maturation.[7,8] Specifically, TC afferents only weakly contact excitatory pyramidal cells and PV cINs during the first postnatal week of development and are later potentiated.[7,9] This developmental plasticity is thought to follow a Hebbian mechanism, in which "cells that fire together, wire together".[10–12] However, homeostatic scaling has also been shown to be critical during development.[13–16] The extent to which these are universal mechanisms or specific to these strengthening processes remains unclear. Remarkably, during the early postnatal week of development, SST cINs transiently receive TC inputs. While the mechanisms underlying transient connectivity are unknown, this early connection is involved in the TC potentiation onto the other cortical neurons.[17,18] As such, SST cINs, which are the earliest born cINs populations, are thought to orchestrate cortical network synchrony during development.[19] Here we explore the mechanisms by which TC inputs weaken onto SST cINs and the molecular players that mediate this process.

In contrast to the means by which TC inputs mature onto PV and excitatory neurons in the somatosensory cortex, we discovered that transient connectivity to SST cINs is inversely correlated with postsynaptic neuron activity level[12,20] and that this process is modulated by metabotropic signaling. We identified the developmental postsynaptic expression of the metabotropic glutamatergic receptor 1 (mGluR1) in SST cINs specifically, as a key player for the TC input transient refinement through the downstream regulation of semaphorin 3A (Sema3A) expression. These results suggest that postsynaptic SST cINs actively regulate

3

circuit development by providing feedback signals, which ultimately underly the proper function of exploratory behaviors in adult mice.

Results

Transient TC connectivity onto SST cINs is input-independent

TC afferents to SST cINs in layer 5 (L5) of the primary somatosensory cortex (S1) are strong during the first postnatal week of development but substantially weakened as maturation proceeds.[17,18] TC inputs to S1 primarily originate from two distinct types of neuron populations, the ventrobasal (VB) and the posterior (PO) nuclei (Figure 1A).[21–25] TC_{VB} and TC_{PO} inputs have distinct functions in adulthood and they also differentially instruct excitatory neuron identity in S1 during development.[26,27] Despite these differences, TC_{VB} and TC_{PO} inputs have similar physiological strength onto postsynaptic SST cINs in adulthood[28,29], suggesting that transient connectivity to SST cINs is independent of their site of origin. To directly explore this hypothesis, we examined TC_{VB} versus TC_{PO} input selectivity onto SST cINs during postnatal development. TC_{VB} and TC_{PO} afferents are interdigitated and they primarily project to L5B and L5A respectively (Figure 1A).[30,31] Using the pan-TC pre- and postsynaptic markers (VGluT2[32] and Homer1 respectively) (Figure 1B), we examined TC synapses to these layers. While their overall densities onto SST cINs decreased over postnatal development (P5, P7 and P30; Figure 1C; Figure S1A-B), we found no significant difference between L5A and B within each stage (Figure 1D), suggesting that TC synaptic refinement onto SST cINs is independent of the afferent thalamic subpopulation. To further characterize the refinement of specific $TC_{VB/PO}$ synapses during development and at maturation (P7 and P30), we performed selective optogenetic stimulation of TC_{VB} and TC_{PO} terminals in L5 of S1 and measured their relative strength onto SST cINs. This was accomplished using mouse driver lines specific for VB and

PO thalamic neurons (Vipr2-Cre[33,34], CR-Cre[35–37] respectively) to activate Cre-mediated AAV-driven opsins (Figure 1E-F; Figure S1C). The monosynaptic excitatory postsynaptic currents (EPSCs) in SST cINs, optogenetically evoked by TC_{VB} or TC_{PO} inputs and normalized by their neighboring pyramidal neuron, were observed to decrease over development. At P7, both TC_{VB} and TC_{PO} inputs evoked larger normalized EPSCs onto SST cINs than those observed onto this same population at P30 (Figure 1G-I; Figure S1D-J).

Together, both anatomical and physiological data showed that the maturation of transient connectivity is associated with weakening and synaptic refinement of both TC_{VB} and TC_{PO} inputs onto SST cINs. The observation that functionally and genetically distinct TC afferents similarly alter the strength of their synaptic inputs on SST cINs during development suggests a postsynaptic role for SST cINs in regulating this process.

Postsynaptic metabotropic signaling in SST cINs regulates the maturation of transient TC inputs

The development of TC projections and cortical topographic maps have been shown to be activity-dependent.[2,35,38,39] More specifically, Hebbian mechanisms, in which "cells that fire together, wire together", are thought to underlie the developmental strengthening of TC inputs onto excitatory neurons.[10–12] Presynaptic activity from TC_{VB} and TC_{PO} inputs, which have distinct genetic and physiological identity[5,6,25–27,40,41], specifically instruct the development of their postsynaptic excitatory neuron target.[26,42] However, the above experiments indicate that transient TC synapses to SST cINs are independent of the origin of their presynaptic inputs. Therefore, we next investigated whether instead postsynaptic activity of SST cINs instead controls TC input refinement. We hypothesized that, similar to Hebbian-based developmental potentiation[9], increasing postsynaptic activity would maintain strong TC inputs onto SST

5

neurons, while decreasing it would promote the normal TC input weakening Accordingly, we used designer receptors exclusively activated by designer drugs (DREADD)[43,44] and the Clozapine-N-oxide (CNO), to either activate (Gq) or inhibit (Gi) SST cINs during the first postnatal week (P0-P8; Figure 2A; Figure S2A)[45,46] and determine how they affected the strength of TC$_{VB}$ inputs onto SST cINs (Figure 2B). Contrary to our expectations, at P10, when the strength of TC inputs onto SST cINs is normally diminished, DREADD-Gq-activation within SST cINs failed to maintain the strength of their TC$_{VB}$ inputs, while Gi-activation within SST cINs strengthened them (Figure 2C-E, S2D-E). After CNO discontinuation (P8), these effects proved temporary, as they were not present anymore by P30 (Figure S2F-G). Consistent with our findings about TC strength at P10, at this time point, Gi(+) SST cINs increased the numbers of TC synapses (VGluT2$^+$/Homer1$^+$) compared to Gq(+) SST cINs (Figure 2F-G; Figure S2H). Notably, neither manipulation altered the density of SST cINs (Figure S2B-C) and their intrinsic properties (Table S1), indicating that changes in their postnatal neural activity levels resulted in no change in apoptosis[49,52,53] or their physiological identity.

We next wished to determine whether the Gi-mediated persistence of strong developmental connectivity was affected as a result of changes in the synaptic homeostasis of SST cINs or other intracellular signaling effects. We therefore examined whether ionotropic-mediated inhibition of SST neuron activity using the Kir2.1 hyperpolarizing potassium channel produced a similar phenotype as that observed upon Gi inhibition. Using SST-FlpO mice and AAV-driven Kir2.1 (fDIO-Kir2.1), we examined whether Kir2.1-mediated inhibition of SST cIN activity altered the optogenetically-induced EPSCs evoked by TC$_{VB}$ inputs (Figure 2H). While Kir2.1 inhibition was previously shown to disrupt TC input refinement and cortical map formation[38,47–52], the chronic hyperpolarization of SST cINs during the first postnatal weeks did not recapitulate the effects observed with TC inputs onto Gi-inactivated SST cINs (Figure 2I-K;

6

Figure S2I-J). Altogether, these results suggest that postsynaptic metabotropic signaling regulates transient connectivity during postnatal development without direct involvement of homeostatic TC synaptic scaling.

mGluR1 is highly expressed in SST cINs during development

To examine whether an endogenous source of metabotropic signaling, comparable to Gq-DREADD, might account for the normal weaking in TC afferents to SST cINs during development, we examined their gene expression during the formation and maturation of TC transient connectivity. Specifically, we analyzed public single-cell RNA sequencing (scRNAseq) data from developing cINs at P2[53] and P10[54]. We aligned the two datasets using canonical correlation analysis (CCA)[55] followed by clustering using the Seurat pipeline.[55,56] We identified cIN types by curating the known inhibitory cIN markers in these cluster populations[54,57] and compared gene expression specific to SST cIN subtype clusters (Figure 3A; Figure S3B)[56] compared to PV or all other cIN types (Figure 3B-E; Figure S3A). Among the three best markers of SST cINs at P2 was Grm1 (Table S3), a gene coding for the mGluR1. mGluR1 expression peaks at P2 and persists in this population from P10 through adulthood (Figure B-E; Table S4).[58–61] Single molecule Fluorescent *In Situ* Hybridization (smFISH) confirmed the colocalization of Grm1 in SST cINs at P2 and P10 in L5 of S1 (Figure 3F). Notably, mGluR1 expression was found to vary within discrete SST cIN subtypes, by P10 in particular (Figure S3B-D).[57] At both stages, the Myh8$^+$ SST cIN population, which is found in L5 of the cortex, as well as the Chodl$^+$ population, exhibit the highest expression of Grm1. These data nominate mGluR1 as a candidate for triggering metabotropic postsynaptic signaling induced by TC glutamatergic activity.

mGluR1 CRISPR-deleted SST cINs retain their strong developmental TC inputs

MGluR1 is a postsynaptic metabotropic receptor primarily coupled with Gq signaling.[62] Based on the high and specific postnatal expression of mGluR1 in SST cINs, we hypothesized that mGluR1-Gq signaling promotes the SST cIN-specific TC input refinement during development. To test this hypothesis, we investigated the function of mGluR1 in weakening of TC transient connectivity using SST cIN specific loss-of-function. To avoid non-cell autonomous effects of the mGluR1 deletion, from thalamic neurons in particular[63], we developed an AAV-based CRISPR strategy to knock down (KD) mGluR1 specifically from SST cINs in S1 (Figure 4A). Grm1 smFISH coupled with SST immunostaining, confirmed the Grm1 transcript depletion from SST cINs at P5 and P10 using the CRISPR strategy (Figure 4B-D; Figure S4A-B). Similar to chemogenetic manipulation of SST cIN activity, mGluR1 KD did not significantly alter the physiological properties of SST cINs at P10 (Table S2). We next examined the maturation of TC$_{VB}$ inputs onto SST cINs in this model. We measured EPSCs from mGluR1 KD SST cINs in response to optogenetic stimulation of TC$_{VB}$ inputs (Figure 4E). At P10, EPSCs of KD SST cINs were larger (Figure 4F-H; Figure S4D-E) than those recorded from control SST cINs (Ctrl). This persistence of developmental TC inputs on SST cINs in absence of mGluR1 was corroborated by an increase of TC synaptic density, as labeled with VGluT2$^+$ and Homer1$^+$ onto KD SST cINs (Figure 4I-J; Figure S4F). The normal TC input weakening never occurred in absence of mGluR1, as EPSC evoked in SST cINs by TC$_{VB}$ remained immature through P30, a stage when S1 is mature (Figure S4G-K).[64] These results reveal that TC synaptic maturation is regulated by postsynaptic SST cIN metabotropic signaling from mGluR1 during development.

This suggests that TC transiently provide inputs to SST cINs during a critical developmental window when sensory activity and SST cINs collaborate to regulate cortical

circuit maturation and assembly. We therefore hypothesized that disrupting early postnatal mGluR1-dependent SST cIN maturation would influence adult circuit function as reflected by behavior. To explore this idea, we characterized the open field behavior of the mGluR1 KD mice, in which the mGluR1 gene is deleted in SST cINs in bilateral somatosensory cortices during the postnatal period (Figure 5A-B). We took advantage of the Motion Sequencing (MoSeq) platform, which identifies and quantifies the use of the brief action motifs (syllables) out of which behavior is organized in a given context (Figure 5C).[65,66] We find that no new syllables are used when comparing the mGluR1 KD with Ctrl mice, but that the distribution of syllables usage was altered (Figure 5D-E). Linear discriminant analysis (LDA) clearly separated Ctrl and mGluR1 KD mice, suggesting clear differences in syllable usage (Figure 5F). We examined the syllables that distinguished Ctrl and KD mice, which revealed a set of 10 syllables that were highly enriched for syllables-related to rearing, related to exploratory behaviors using sensory cues. We repeated LDA on subsets of sessions and further identified two groups of syllables that robustly distinguished Ctrl and KD mice across iterations by sex. The use of these syllables alone could predict whether a given mouse was a Ctrl or a KD mouse well above chance (Figure 5G). These data demonstrate that deficits in mGluR1 function in SST cINs, which we have shown lead to pervasive developmental phenotypes, are associated with significant sensory exploration behavioral phenotypes as identified by an unsupervised analysis. We verified that these behavioral dysfunctions did not originate from cell death or extensive cortical rewiring, downstream of TC input maturation to SST cINs. While postsynaptic mGluRs have been shown to prevent cell death[67], the postnatal mGluR1 CRISPR deletion did not induce significant change in the number of infected SST cINs at P30 (Figure S4C). Furthermore, anatomical neural pathways connecting to SST cINs using monosynaptic retrograde rabies tracing were normal, including the adult organization of TC pathways (Figure

9

S5).[40,41] These results suggests that mGluR1 in SST cINs regulates the proper maturation of adult cortical functions primarily through synaptic refinement, rather than gross anatomical developmental events.

mGluR1-dependent Sema3A expression controls TC transient connectivity onto SST cINs

MGluRs do not only modulate postsynaptic neuron activity, but have also been shown to regulate gene transcription[68] and translation[62,69]. We therefore hypothesized that chronic activation of mGluR1 by TC inputs during the first postnatal week of development modulates transcriptional levels of genes regulating synaptic maturation. Semaphorin (Sema) 3A and 7A have been shown to mediate feedback signaling in the cerebellum[70] and mGluR1 pathways have been shown to regulate their activity in several brain regions.[70,71] Therefore, we investigated whether Sema3A and Sema7A are expressed in SST cINs during development using the integrated P2/P10 scRNAseq. In contrast to Sema7A (Figure S6A), Sema3A is highly expressed at P2 and P10 in SST cINs (Figure 6A). Secreted Sema3A primarily acts as a repulsive guidance cue of axons, notably through Plexin A1 interactions.[72–74] We examined the expression of Plexin A1 in the thalamus using the Allen *in situ* hybridization developing mouse brain atlas[75] and found similar dynamics of Plexin A1 expression as Sema3A (Figure S6B). Thus, in terms of both Sema3A in SST cINs and its cognate receptor in TC afferents, the timing of their expression is consistent with these functioning to mediate mGluR1-mediated downregulation of TC inputs to SST cINs.

To further test this hypothesis, we investigated whether Sema3A transcription is regulated by mGluR1. Using smFISH quantification of Sema3A in Ctrl and mGluR1 KD SST cINs, we revealed that Sema3A transcripts are downregulated in absence of mGluR1 (Figure

6B-C; Figure S6C). Second, we examined whether Sema3A is necessary to control the maturation of TC transient connectivity onto SST cINs. To do so, we used a similar CRISPR strategy to knock down Sema3A from SST cINs and measured TC$_{VB}$ input strength onto Sema3A KD and Ctrl SST cINs (Figure 6D). At P10, both the normalized amplitude and charge of Sema3A KD SST cIN responses were up to five times bigger than Ctrl SST cINs (Figure 6E-G; Figure S6D-F). Altogether these results show that Sema3A expression is regulated by mGluR1 and is a key feedback regulator of the transient connectivity between TC inputs and SST cINs (Figure 7).

Discussion

TC afferents to pyramidal and PV neurons become strengthened as development proceeds through Hebbian mechanisms. In contrast, here, we show that early TC connectivity onto SST cINs recruits mGluR1-based transcription, supporting the later elimination of this connectivity known to regulate the development of cortical networks.[17,18] [17,18] Interestingly the removal of mGluR1 signaling from SST cINs during this critical period also impacts the development of normal sensory-related behaviors.

SST cINs in L5 of S1 are among the earliest born populations within this region. Previous works, including from our laboratory, have demonstrated that they play a critical developmental role in regulating the PV cIN maturation and the formation of the feedforward inhibition to pyramidal neurons.[18] These works, in combination with our present findings, illustrate that SST cINs play a key role in regulating the maturation of S1 cortex that is distinct from those involving Hebbian or homeostatic plastic mechanisms utilized to shape the TC afferents to other cortical neurons. Instead, here, we demonstrate that the dynamic connectivity of TC inputs is regulated through SST cINs using mGluR1-dependent Sema3A expression to directly weaken TC inputs

during postnatal development, when S1 cortex begins to assume its mature function. The discovery of this mechanism illustrates how genetically-programmed signals within the SST cIN population allows the thalamic afferents to activate a critical developmental signal that reconfigures S1 cortical circuits. During this period, SST cINs hand over the bottom-up FFI from the thalamus to PV cINs and in turn assume their adult role in regulating local feedback signaling to L5 pyramidal neurons. Hence, in contrast to the typical activity-based mechanism by which network dynamics drive cortical maturation, the L5 SST cINs provides a critical signaling mechanism that initiates the transition from developmental bottom-up signaling to the critical period rebalancing of bottom-up and top-down cortical functions in S1 cortex.

The feedback mechanism of sensory TC transient connectivity onto SST cINs occurs during critical periods of plasticity, when somatosensory topographical maps are highly sensitive to sensory TC inputs.[76,77] In addition, SST cINs have been directly involved in inducing these critical periods of plasticity in the visual cortex.[78,79] Therefore, our findings provide a potential genetically-encoded mechanism, by which SST cINs controls TC input-driven cortical plasticity and ultimately somatosensory cortical functions. Notably, this mGluR1-based feedback mechanism is specific to development, as mGluR1, which remains largely specific to SST cINs at adulthood, has been shown to trigger SST cIN potentiation in adult prefrontal cortex.[61] The opposite effects of mGluR1 at different stages, suggests a distinct SST cIN specific molecular context, such as Sema3A expression, controlling age-dependent functions. Moreover, this highlights the essential role of these developmental programs, rather than adult plasticity mechanisms for the formation of proper adult cortical circuits.

It remains to be determined whether these developmental genetic programs in SST cINs are sufficient to instruct feedback transient connectivity and input/output circuit reorganization. Interestingly, our postnatal scRNAseq analysis revealed that mGluR1 is also expressed

developmentally in VIP cINs (Sncg[+] and Vip[+] cIN clusters; Figure 3A&D), which have been shown to receive transient TC inputs during development.[80] Therefore, mGluR1 is a strong candidate for intrinsic encoding of developmental transient TC connectivity and bottom-up/top-down circuit wiring. The model in which cell type genetic identity is sufficient to determine feedback TC input maturation provides for a powerful framework to generates circuit diversity from common TC afferents, such as the formation of feedforward versus feedback inhibition formed by PV and SST cINs respectively.

Guidance molecules are responsible for circuit wiring and are generally associated with global axon growth during embryonic development.[81] In contrast, postnatal activity-dependent mechanisms of pruning and strengthening are usually linked to neurotransmitter receptors and their composition.[39,77,82] Here, our results reveal a tight interplay between these two mechanisms. Linking neural activity with genetic programs of development is essential for a better understanding of neurodevelopmental disorder etiologies. Indeed, a lack of general synaptic refinement has been associated with autism spectrum disorders (ASD).[83,84] In addition, disruption of transient brain structures and defects in inhibitory and excitatory balance have been found in autism spectrum disorders (ASD) in particular.[85] However, the role of TC transient connectivity to SST cINs in cortical dysfunctions found in neurodevelopmental disorders remains unexplored.

STAR*Methods

RESOURCE AVAILABILITY

Lead contact

Further information and requests for resources and reagents should be directed to and will be fulfilled by the Lead Contact, Gabrielle Pouchelon (pouchel@cshl.edu).

13

Materials availability

All plasmids generated for this paper were designed and cloned for CRISPR strategy and are available upon request.

Data and code availability

- All quantified data are available in main, supplementary figures and supplementary tables. All original physiological, imaging, histological data are archived at Harvard Medical School Fishell lab server and Cold Spring Harbor Laboratory, Pouchelon lab server. Any additional information required to reanalyze the data reported in this work paper is available from the Lead Contact upon request.

Experimental Model and Subject Details

Mice. All experiments were approved by and in accordance with Harvard Medical School IACUC protocol number IS00001269 and by Cold Spring Harbor Laboratory IACUC protocol number 22-4. Animals were group housed and maintained under standard, temperature-controlled laboratory conditions. Mice were kept on a 12:12 light/dark cycle and received water and food *ad libitum*. C57Bl/6 mice were used for breeding with transgenic mice. Transgenic mice, SST-Cre (stock number: 013044)[35], SST-FlpO (stock number: 031629)[86], Vipr2-Cre-neo (stock number: 031332; RRID:IMSR_JAX:031332)[87], Calb2-Cre (stock number: 010774; RRID:IMSR_JAX:010774)[35], LSL-Cas9-eGFP (stock number: 026175)[88], RCE:LoxP (stock number: 032037)[89], PV-Cre (stock number: 017320; RRID:IMSR_JAX:017320)[90] are available at Jackson Laboratories. Mice were injected at P0 and experiments conducted between ages P3-P10 for developmental stages and between ages P28-37 for adult/mature time points. Both female and male animals were used for all experiments.

METHOD DETAILS

Histology

Immunohistochemistry (IHC) - Mice were deeply anesthetized with sodium pentobarbital by intraperitoneal injection and transcardially perfused with PBS 1X followed by paraformaldehyde (PFA) dilutes at 4% in PBS. Brains were postfixed for 4 hrs in 4% PFA at 4 °C, except for monosynaptic rabies tracing, for which brains were postfixed overnight. 50 μm vibratome (Leica) sections were incubated 1-2 hrs at room temperature in a blocking solution containing 3% Normal Donkey serum and 0.3% Triton X-100 in PBS and incubated 48 hrs at 4°C with primary antibodies: rat anti-RFP (1:1,000; Chromotek #5f8), chicken anti-GFP (1:1,000; Aves Labs #1020), rabbit anti-Homer1b/c (1:500, Synaptic Systems #160023), guinea-pig anti-VGlut2 (1:2000, Millipore #AB2251), guinea-pig anti-VGlut2 (1:1000, Synaptic Systems #135404), rabbit anti-somatostatin (1:3,000; Peninsula Laboratories International T-4103.0050) and rabbit anti-mGluR1a (1:1000; Af811 Frontier Institute, RRID:AB_2571799), which exhibits the best labeling compared to multiple anti-mGluR1 we tested (negative controls in constitutive mGluR1 KO did not show any signal, data not shown). Sections were rinsed three times 15 min with 0.1% Triton X-100 in PBS and incubated for 60–90 min at room temperature or overnight at 4°C with Alexa Fluor 488- , 594- or 647-conjugated donkey secondary antibodies (1:500; Thermo Fisher Science or Jackson ImmunoResearch). Sections were mounted in Fluoromount-G (Southern Biotechnology, #100241-874) before imaging.

Dual single molecule Fluorescent In Situ Hybridization (smFISH) and Immunohistochemistry (IHC) - For combined smFISH and IHC, mice were deeply anesthetized with sodium pentobarbital by intraperitoneal injection and transcardially perfused with PBS followed by 4% PFA. Brains were fixed 1hr at room temperature and 2hrs in 4% PFA at 4 °C. The brains were cryopreserved in 30% sucrose before sectioned at 20 μm using a sliding microtome (Leica).

15

Sections were stored in a cryo-solution containing 28% (w/v) sucrose, 30% (v/v) ethylene glycol in 0.1M sodium phosphate buffer, pH 7.4, before performing smFISH experiments. RNAscope® fluorescent *in situ* hybridization and immunohistochemistry (Dual FISH-IHC) assay was performed using RNAscope® Multiplex Fluorescent Detection Kit v2 (ACDBio 323110) purchased from Advanced Cell Diagnostics (ACDBio). Manufacturer's protocol for fixed frozen tissue was followed. Probes used in this study include Mm-Grm1 (ACD 449781), Mm-Sema7A (ACD 437261-C3), Mm-Sema3A (ACD 412961). After smFISH, IHC was performed. Sections were washed in Tris-buffered saline, pH 7.4, (TBS) with 10% Tween®20 (TBST) and blocked in 10% Normal donkey serum in TBS-0.1% Bovine serum albumin (BSA) for 1 hour at room temperature. Primary antibodies, rat anti-RFP (1:1,000; Chromotek #5f8) to reveal AAV-sgRNA-DIO-dTomato reporters, and rabbit anti-somatostatin (1:3,000; Peninsula Laboratories International T-4103.0050) diluted in TBS-0.1% BSA, was applied to the sections for 2 hours at room temperature. Sections were washed in TBST and incubated in corresponding Alexa-conjugated secondary antibodies (1:500; Thermo Fisher A-10040), in TBS-0.1% BSA, for 1 hour at room temperature. Sections were washed in TBST and DAPI (5 uM; Sigma D9542) was applied to each section for 30 seconds. Prolong Gold antifade mounting medium (Thermo Fisher P36930) was used to adhere glass coverslip.

Mouse neonate stereotactic injections

For postnatal time points stereotaxic injections were possible using a neonate adaptor (Harvard apparatus). Mouse pups were anesthetized by hypothermia 5 min and stereotaxically micro-injected with AAV (volume 80-100 nl) at P0-P1 with a micro-injector (Nanoject III). Primary somatosensory cortex (S1) was targeted with the following coordinates: AP+1.40, ML-1.85, DV-0.20 from Lambda. For slice physiology experiments, double injection of in S1 cortex and the somatosensory thalamus of Vipr2-Cre or Cab2-Cre mice were performed at P0. Thalamus

16

coordinates for VB and PO were as follows: AP+0.9, ML-1.0, DV-2.4 from Lambda. For more consistent targeting, cortical injections were performed over 5 min and thalamic injections over 10 min, following a 20 nl, 4-5 time with 10s delay program. After surgery, mice were given Meloxicam (Metacam) subcutaneously at 5 mg/kg of body weight and, upon recovery on a heating pad set at 37 °C, were placed back in the home cage with the mother.

Chronic DREADD activation

For DREADDs experiments, Clozapine-N-Oxide (CNO, Tocris) or CNO dihydrochloride (Hello Bio) was dissolved in 5% dimethyl sulfoxide (Sigma) or 0.9% saline respectively, at 1 mg/ml (10x solution) and stored at 4 °C for the duration of the chronic activation (7 days). Every day, fresh 1x CNO solution was made by fresh dilution with 0.9% saline to 0.1 mg/ml. Pups were injected with CNO (10 ul/g equivalent to 1 mg/Kg) subcutaneously for 7 days (from P1-P8), twice daily.

Adult stereotactic injections

For monosynaptic rabies retrograde labeling, stereotactic injection of EnVA-CVS-N2c-dG-H2B-tdTomato (70 nL; dilution 1/10, Addgene plasmid: #175441) [51] was performed at P30 in animals previously injected with AAV-3xgRNA-DIO-TVA-N2cG at P0 (80 nl), using a Nanoject III at 1 nl/second according to stereotaxic coordinates (from Bregma AP+1.00, ML-3.00, DV-0.89). Animals were perfused 7 days later and processed for immunohistochemistry.

Viruses

The enhancers, reporters, and effectors were cloned using the Gibson Cloning Assembly Kit (New England BioLabs, catalog no. NEB-E5510S). After cloning and sequencing, the growth time of the transformed DH10B Competent Cells was kept below 12 hours on plates and 10 hours in flask at 37 C. DNA from several clones was recovered with an endotoxin free midi-kit (Zymo D4202). This allows for consistently obtaining low recombination rates detected by PCR.

Primers were designed for amplification of plasmids at the junction of each possible recombined form and compared to recombination-free controls. Only clones with a recombined/not recombined ratio of 1.0E+05 or greater were considered for further AAV production. The rAAVs were produced using standard production methods. Polyethylenimine was used for transfection and OptiPrep gradient (Sigma) was used for viral particle purification. Titer was estimated by quantitative PCR with primers for the WPRE sequence that is common to all constructs.

AAV2/1-hSyn-fDIO-DREADD-Gi-mCherry and hSyn-fDIO-DREADD-Gq-mCherry were produced from gifts from U. Gether (http://n2t.net/addgene:154867/addgene #154867; http://n2t.net/addgene:154868/#154868). Titer: 1.80E+12 and 1.72E+12 vg/ml.

AAV2/1-hSyn-DIO-DREADD-Gi-P2A-tagBFP and DREADD-Gq-P2A-tagBFP were generated from VTKS2 backbone[91] and produced for this manuscript. Titer: 3.6E+12 and 9.1E+11 vg/ml.

AAV8-hSyn-DIO-HA-hM3D(Gq)-IRES-mCitrine and -HA-hM4D(Gq)-IRES-mCitrine were gifts from B. Roth (http://n2t.net/addgene:50454/addgene #50454-AAV8; http://n2t.net/addgene:50455/addgene #50455-AAV8). Titer: 1.9E+13 and vg/ml.

AAV2/1-3x Grm1 gRNA-DIO-dTomato was generated from the VTKS2 backbone and produced for this manuscript. Titer: 2.42E+12 vg/ml.

AAV2/1-3x Grm1 gRNA-DIO-N2cG-TVA was generated and produced for this manuscript. Titer: 7.8E+12 vg/ml.

AAV2/1-3x Grm1 gRNA-fDIO-dTomato was generated from the VTKS3 backbone and produced for this mansucript. Titer: 2.0E+12 vg/ml.

AAV2/1-3x Sema3a gRNA-DIO-mCherry was generated from the VTKS2 backbone and produced for this manuscript. Titer: 1.07E+12 vg/ml.

AAV2/9-Ef1a-DIO-ChRmine-mScarlet was produced by the Children's Hospital Viral Core from a plasmid, which was a gift from K. Deisseroth[92] (http://n2t.net/addgene:130998/addgene#130998) produced by. Titer 6.26E+14 vg/ml.

AAV2/1-DIO-mCherry was generated from the VTKS2 backbone and produced for this manuscript. Titer: 1.4E+12 vg/ml.

AAV PHP.eB-EF1a-DIO-hChR2(H134R)-eYFP and AAV9-EF1a-fDIO-eYFP were gifts from K. Deisseroth (http://n2t.net/addgene:20298/addgene #20298-AAV-PHPeB[93]; http://n2t.net/addgene:55641/addgene #55641-AAV9)[94]. Titer: 1.00E+13 and 2.00E+13 vg/ml.

AAV2/1-hSyn-fDIO-HA-Kir2.1 was generated from the VTKS3 backbone and produced for this manuscript. Titer: 2.60E+12 vg/ml.

AAV9-EF1a-fDIO-Cre was a gift from E. Engel & A. Nectow[95] (http://n2t.net/addgene:121675/addgene #121675-AAV9). Titer: 2.50E+13 vg/ml.

AAV-PHP.eB-S5E2-dTomato was a generous gift from J. Dimidschstein. Titer: 8.3E+09 vg/ml.[96]

EnvA-pseudotyped CVS-N2c(deltaG-H2B:tdTomato) Rabies construct that we previously generated (Addgene #175441)[97] was utilized for monosynaptic retrograde labeling. Titer: 3.7E+09U/ml. The nuclear labeling from H2B:tdTomato improves the automated cell detection and the overall accuracy. Rabies were generously shared by K. Ritola. Titer: 1.4E+08U/ml.

CRISPR strategy

For proper deletion of Sema3A and Grm1 genes, three guide RNAs (gRNA) were packaged into one single AAV. Each gRNA is under human U6 promoters and with a scaffold gRNA and a polyA sequence at their 3' end. The whole triple gRNA (3x gRNAs) construct was synthesized by GeneScript with an ApaI site at each end, to be directly inserted into a VTKS2 or VTKS3

AAV backbone[91], upstream of the human Synapsin promoter, which controlled a DIO- or a fDIO-reporter (dTomato or N2cG rabies helpers). Each 3x gRNA was packaged into single AAV1. Grm1 gRNA with spCas9 PAM sequences were designed by cross-validating best ON- and OFF-target scores from Benchling CRISPR gRNA Design Tool, ChopChop[98,99] and CRISPick (previously known as Genetic Perturbation Platform (GPP)). gRNA suggestions were picked in Exons 1 to 3, to increase the probability of full gene deletion. Sequence of selected Grm1 gRNAs are: 5'-CGATGCTTGATATCGTCAAG-3'; 5'-CGACCGCGTCTTCGCCACAA-3' and 5'-GTCGCTCAGGTCTATGCTCG-3'. Sequence selected for Sema3A gRNAs are: 5'-TACTCCGTTCTTCATCCAGA-3'; 5'-TGTGGCCAGTATCTTACACA-3'; 5'-GAGACGTTAGTGTTGCCATG-3'.

Of note, since each guide have their own off-target effects, it has been increasingly accepted that scrambled gRNAs are not proper controls for CRISPR, in contrast to shRNA or siRNA. In this manuscript, Cas9(+) or animals without gRNA infection were considered as controls. Alternatively, gRNA-DIO-reporter(+) cells were used as controls. In electrophysiology experiments, Vipr2-Cre mouse line was utilized for opsin expression in the thalamus. Vipr2-Cre recombination is specific to the first-order thalamus and practically absent from the entire cortex (Allen Brain Atlas Transgenic Characterization)[75], preventing Cas9 recombination in non-SST cINs. Moreover, SST-Cre alone was not sufficient to trigger Grm1 deletion by P5 and P10, when injected at P0 (Data not shown). Therefore, we used a combination of Vipr2-Cre and SST-FlpO mouse lines, together with an AAV-fDIO-Cre and the AAV-sgRNAs to trigger CRISPR-deletion in SST cINs early in postnatal development.

10x single cell RNAseq

Publicly available scRNAseq datasets for P2 and P10 cINs were used[53,54] (Gene

Expression Omnibus (GEO) at accession number GSE165233 and GSE104158, respectively). P2 scRNAseq was obtained from Dlx6a-Cre; Ai14(+) sorted cINs and prepared with 10x v3.1 Genomics Chromium platform, with a total of 5,384 cells sequenced. P10 scRNAseq was obtained from Dlx6a-Cre; RCELoxP sorted cINs and prepared with 10x Genomics Chromium system, with a total of 6,346 cells sequenced. While public data are already processed, we aligned the same and higher quality criteria to both datasets, by removing cells with a number of UMI of 500 minimum and 10,000 maximum and cells with higher than 10% mitochondria. Clustering of both datasets was performed using Seurat pipeline in "R"[55]. The number of principal components used for clustering analysis were determined with the ElbowPlot function (20 dimensions). Cells within P10 and P2 were assigned to cIN type via Seurat canonical correlation analysis (CCA) and clusters assigned based on gene marker expression.

Cells within non-cIN clusters (excitatory neurons and glial cells) were defined based on the expression of their developmental markers[100] and removed from the UMAP representation (data not shown; Slc17a7, Neurod6, Mki67, Mbp, Gfap).

Marker expression of cIN types were defined as described in[54] for the main cIN types (such SST and PV cINs) and supported with [57] to assign SST cIN subpopulations (such as Myh8+ and Chodl+ SST cINs). Marker genes for early postnatal PV cINs are: Mef2c, Erbb4, Plcxd3, Grp149; marker genes for early postnatal SST cINs are: Sst, Tspan7, Satb1. For subpopulations, we verified the expression of adult marker genes in the integrated P2-P10 datasets. SST cIN subtype marker genes expressed at P2/P10 are: Cbln4 (T-shaped Martinotti cINs), Hpse (L4-projecting cINs), Myh8 (T-shaped Martinotti cINs), nNos1/Chodl (long-range projecting cINs).

Using Seurat, we performed differential gene expression (DGE) between identified SST cIN and PV cIN clusters, between SST cINs and all other cIN clusters, and between SST-Myh8

subtype with all other cIN subtypes, based on the non-parametric Wilcoxon rank sum test. Log2 (fold change(FC)) and adjusted p-values of the top candidates are represented in Table S3 and S4. Adjusted p-values smaller than 2.22E−16 cannot be computed by "R". For visible volcano plot representations, a constant corresponding to one-digit value lower than the last positive decimal of the lowest computer p-value, as added to p-values = 0. Comparisons were done at each age, P2 and P10, separately.

Whole-cell slice electrophysiology

For P6-7 time point, injection of DIO-Chrmine at P0 generated stronger TC input stimulation and improved optogenetic variability from the restricted AAV-expression in such short time windows. From P10 throughout adulthood, DIO-ChR2 was sufficient to evoke more consistent responses. P6-7 mice were anesthetized by hypothermia, followed by decapitation. P10 and P30 mice were anesthetized using isoflurane, followed by decapitation. Brains were dissected out in ice-cold oxygenated (95% O_2 and 5% CO_2) sucrose cutting solution containing (in mM): 87 NaCl, 2.5 KCl, 2 $MgCl_2$, 1 $CaCl_2$, 1.25 NaH_2PO_4, 26 $NaHCO_3$, 10 glucose and 75 sucrose (pH = 7.4). 300-µm thick coronal slices were cut using a Leica VT1000S vibratome through the primary somatosensory cortex. Slices recovered in a holding chamber with artificial cerebrospinal fluid (ACSF) containing (in mM) 125 NaCl, 20 Glucose, 2.5 KCl, 1.25 NaH_2PO_4, 26 $NaHCO_3$, 2 $CaCl_2$, 1$MgCl_2$ (pH = 7.4) at 32°C for 30 minutes and room temperature for at least 45 minutes prior to recordings. For recordings, slices were transferred to an upright microscope (Scientifica) with oblique illumination Olympus optics. Cells were visualized using a 60x or a 20x water immersion objective. Slices were perfused with oxygenated ACSF in a recording chamber at room temperature at 1-2 ml/min. Recording electrodes (3–6 MΩ) were pulled from borosilicate glass (1.5 mm OD, Harvard Apparatus) with a horizontal P-1000 Flaming Micropipette Puller (Sutter Instrument). For current-clamp recordings, electrodes were

filled with an internal solution containing (in mM): 130 K-Gluconate, 10 KCl, HEPES, 0.2 EGTA, 4 MgATP, 0.3 NaGTP, 5 Phosphocreatine and 0.4% biocytin, equilibrated with KOH at pH = 7.4. For voltage-clamp recordings, electrodes were filled with an internal solution containing (in mM): 125 Cs-gluconate, 2 CsCl, 10 HEPES, 1 EGTA, 4 MgATP,0.3Na-GTP,8 Phosphocreatine-Tris, 1 QX-314-Cl, equilibrated with CsOH at pH = 7.4. Recordings were performed using a Multiclamp 700B amplifier (Molecular Devices) and digitized using a Digidata 1550A and the Clampex 10 program suite (Molecular Devices) or, using an EPC 10 amplifier (HEKA) and the Patchmaster software (HEKA). Voltage-clamp signals were filtered at 3 kHz and recorded with a sampling rate of 10 kHz. Recordings were performed at a holding potential of -70 mV. Cells were only accepted for analysis if the initial series resistance was less than 40 MΩ and did not change by more than 20% during the recording period. The series resistance was compensated at least ~50% in voltage-clamp mode, and no corrections were made for the liquid junction potential. Whole-cell patch clamp recordings were done from reporter-expressing SST cINs and nearby non-fluorescent pyramidal neurons in L5. fDIO-mCherry was used for developmental analysis and all control conditions throughout the study. Pyramidal neuron recordings were used to normalize the SST cIN recordings. To stimulate thalamic afferents expressing ChR2, blue light (5.46-6.94 mW from the objective) was transmitted from a collimated LED (Mightex) to the epifluorescence port of the microscope. We used a 5 ms pulse of light for the stimulation of P7 and P10 slices and a 1 ms pulse of light for P30 slices. Pulses were delivered once every 5 s, for a total of 15 trials. To isolate monosynaptic EPSCs from thalamus to cortex, recordings were performed in the presence of 1 µM TTX and 1 mM 4-AP (Tocris). Data analysis was performed using MATLAB and Prism 8 (Graphpad). The peak amplitude of the evoked EPSCs were averaged across the 15 trials per

cell. EPSC amplitude for the SST cINs was normalized to the EPSC amplitude evoked in the nearby pyramidal neurons to normalize the variability in the injection size between animals. For intrinsic properties, SST cINs were recorded in current-clamp mode and the data were acquired at 20 KHz. In supplementary Table 1, Resting Membrane Potential (RMP) of the cell is the potential when the net injected current (holding current + IV current-clamp step) is the closest to zero. Input Resistance (IR) was computed using Ohm's law ($V = I/R$) by finding the slope of the IV curve obtained using the net current from the IV current-clamp protocol sweep with no action potential (AP) and the potential from the corresponding sweeps. Rheobase was defined as the minimum net injected current to evoke a sweep with more than one AP. AP threshold was defined as the max of the second derivative of the first AP from the first sweep with more than one AP. In supplementary Table 2, Resting Membrane Potential (RMP) of the cell was recorded as mean membrane potential from a 1 min long recording in I = 0 mode or by taking the mean potential from . Input Resistance (IR) was computed using Ohm's law ($V = I/R$) by finding the slope of the IV curve obtained using current injection from -10 to 10 pA in steps of 5 pA. Rheobase was defined as the minimum input current to evoke firing from a cell. Spike threshold was defined as the membrane potential where dv/dt > 5 mV/ms before spike initiation. mGluR1 KD intrinsic properties analysis were compared to publicly available Control data of SST cINs in somatosensory cortex at P10, recorded the same way.[97] Analyses were done using clampfit, Easy electrophysiology and Python. Statistical analyses were done using Python (scipy)[101] and in GraphPad prism 9.

Motion Sequencing (MoSeq)

SST-Cre:Cas9fl mice were injected with AAVs expressing mGluR1-gRNA, fDIO-Cre bilaterally in the somatosensory cortex at P0-P1. Control animals were SST-Cre:Cas9fl injected with fDIO-Cre-AAV or gRNA-AAV only, or SST-Cre animals injected with both fDIO-Cre- and gRNA-

AAVs. All mice were perfused after recording and analysis to confirm the bilateral targeting of the somatosensory cortices, as in Figure 5B. Mice were recorded around 2.5 months of age. MoSeq recording were carried out as previously described.[65,66] 3D depth video is recorded in a circular 17'' diameter open-filed arena (OFA) using a Microsoft Kinect v2 depth camera. Briefly, mice were freely moving in the arena for 45 mins in the dark, and put back to their home cage. The arena is wiped down with 10% bleach, followed by 70% ethanol between each session. After removing corrupted sessions due to a significant amount of noise in the recording, in total 44 female mice (24 Ctrl and 20 KD) and 32 male mice (20 Ctrl and 12 KD) were used in the analysis.

MoSeq is an unsupervised machine learning algorithm that segment animal behavior into repeated modulated motifs called syllables. MoSeq pipeline (http:www.moseq4all.org) takes 3D depth videos as input and produces frame by frame syllable labels for each frame in the videos. Depth videos first goes through image processing in MoSeq package suite to crop out and align the mouse such that the center of the mouse is at the center of the frame, and the nose of the mouse is pointing right. To accommodate noise and morphological variations, the processed aligned video goes through a deep neural network for denoising. The denoised data goes through dimensionality reduction and modeling step to generate the syllable labels. Syllables are labeled by sorted usage across all sessions such that syllable 0 is the most used syllable and the syllables make up 99% of the total frames are included in the analysis. Syllable usages by group are aggregated across all sessions in the group (i.e. male Ctrl, male KD, female Ctrl, female KD) and normalized such that syllable usages within one session add up to 1. Chi-square tests are done on the unnormalized frame counts aggregated by group.

Linear Discriminant Analysis (LDA) - To find the syllables that distinguished Ctrl from KD animals, we used LDA on syllable usages across all sessions to find the linear projection that

25

maximizes group separability between Ctrl and KD mice, and sessions from both male and female data in each genotype are combined.

To find a set of syllables that robustly distinguish Ctrl and KD mice by sex, we applied leave-one-out strategy and trained multiple LDA embedding on a subset of the sessions within the same sex, leaving one session out. The top 10 high absolute loading syllables are recorded at each iteration and the most frequent 10 syllables among all the iterations by sex are used in the linear classifier.

Linear Classifier on syllable usages- We applied a linear classifier to the usages of the subset of syllables identified in the leave-one-out LDA described above. Since the number of Ctrl and KD mice included in both males and females are unbalanced, the data is randomly subsampled such that both Ctrl and KD have the same number of mice. The subsample process is repeated 10 times. After subsampling, the input data goes through a standard scaler for data preprocessing, and logistic regression is used to predict genotype. Leave one out cross validation is used to compute model accuracy.

Quantification and statistical analysis

All statistical details can be found both in the results and the legends of the corresponding figure. In the manuscript, "N" represents the number of animals, while "n" represents the number of cells. All statistical analyses were performed using GraphPad Prism, Python (scipy) and R software. Unless otherwise tested, statistical significance was tested with one-way ANOVA, followed by post-hoc Tukey's multiple comparison test or Student t-test for parametric data and with one-way Kruskal-Wallis followed by post-hoc Dunn's test or Mann-Whitney test for non-parametric data. P values < 0.05 were considered statistically significant. For all figures, *p < 0.05; **p < 0.01; ***p < 0.001; ****p < 0.0001.

The normal distribution of the synaptic density was formally tested with a Kolmogorov-Smirnov test. The data distribution was normal during development and we used parametric statistical tests, as also applied in previous studies of postnatal synaptic quantification.[102] The distribution of the synaptic density in CRISPR KD and DREADD experiments did not show a normal distribution and were tested with non-parametric tests.

The data distribution of cell density and monosynaptic retrograde labeling was assumed to be normal and analyzed with parametric tests, based on previous studies[52], but was not formally tested.

RNA particle distribution (from smFISH) appears to be marker-specific, as previous studies use parametric and non-parametric tests. We formally tested the data distribution of Grm1 RNA particles, found they are primarily normal (with D'Agostino Pearson test. The exception was P10 data, when tested with a Kolmogorov-Smirnov test only, p-value = 0.0132) and used parametric tests. In contrast, Sema3A smFISH data distribution was not normal (Kolmogorov-Smirnov test p-value <0.0001) and non-parametric tests were performed.

The data distribution of optogenetics responses was assumed to be non-gaussian[4,103,104] and analyzed with non-parametric tests, based on previous studies, but was not formally tested.

Image acquisition and analysis

For all analyses, images were taken in layer 5 of the somatosensory cortex, except for cell number quantification, which was performed in all layers. For analysis of synapse density and smFISH, tissue samples were imaged on an upright ZEISS LSM 800 confocal using a 40X oil immersion objective, 1.4 NA, 2.5 digital zoom, 2,048 x 2,048 pixels, 16 bits. For cell density and monosynaptic retrograde labeling, tissue samples were imaged on a ZEISS Axio Imager using a 10X dry objective (with tiling mode).

Synaptic density - For TC synapse analysis onto PV and SST cINs, single planes were analyzed using a custom script in Fiji (ImageJ) software, as previously described before [107]. In brief, noise reduction and smoothing were applied to all channels and imaged converted to RGB. A color threshold was automatically set to identify the cell body of SST cINs and PV cINs labeled with the RCELoxP mouse line. In contrast, the reporter distribution of DREADD-Gi/Gq and as well as the somatostatin labeling were not homogeneous. In that case, manual delimitation of cell bodies was performed. Cell body perimeter was automatically measured and a masked binary image with the cell body only was created. For bouton segmentation, a watershed-based method is used such that boutons were separated based on the local minima of the pixel gray values. For the presynaptic boutons (VGluT2) and postsynaptic clusters (Homer1), a color threshold was selected to segment boutons as isolated puncta. The comparison between the original images and the masks was used to guide the choice of the threshold value, which was determined to detect all putative presynaptic boutons or postsynaptic clusters in each condition. The ''Analyze Particles'' (VGluT2 minimum size = 0.20 mm; Homer1 minimum size= 0.10mm) and ''Watershed'' tools were applied and a mask was generated. A merged image from all masks was created, converted to an 8-bit image and the overlap between presynaptic TC puncta, postsynaptic clusters and the cell body was automatically detected.

smFISH analysis - single RNA molecules were quantified within SST cINs, as labeled with somatostatin antibody. Control cINs were imaged in the non-injected contralateral side, while KD cINs were imaged in the injected ipsilateral side and identified by the AAV-reporter colocalization. Single plane images were analyzed using a similar adapted custom script in Fiji (ImageJ) software. Images were converted in RGB, cell bodies first identified as control or KD and then manually delimited based on the somatostatin labeling. Grm1 RNA, in particular,

28

formed dense clusters within the cells and the watershed-based method was used to separate particles. A color threshold was applied to all images of the same condition to segment RNA particles. The "Analyze Particles" (minimum size for Grm1 was determined as ~ 0.30 mm) and "Watershed" tools were applied and a mask was generated. A merged image of the 2 masks was created, converted to an 8-bit image and the overlap between SST cINs and RNA dots automatically detected.

Cell density - For SST cIN density in DREADD experiments at P10, SST cINs were labeled with the AAV-DIO-reporter, mCitrine for DREADD-Gi/Gq. SST cIN infected with AAV-DIO-DREADDGi-mCitrine, from mice injected with saline instead of CNO, were the control condition. For SST cIN density in mGluR1 KD CRISPR experiments at P30, SST INs were identified from the LSL-Cas9eGFP labeling. Control cINs were infected by fDIO-Cre only without AAV-sgRNA. Using Fiji (ImageJ) software, areas covering ~ 3-4 topographical columns of the somatosensory cortex were drawn from layer 1 to the white matter. Area (mm^2) was measured to normalized cell number and SST cINs were manually counted using the "cell counting" plugin. Quantification of 1-to-3 sections per DREADD(+) and 4 sections per CRISPR KD and Ctrl brains were averaged to represent 1 biological N each. The identification of each condition was blind to the experimenter.

Monosynaptic retrograde labeling quantification - Every 4th section of a whole brain (from orbital cortex to brainstem) was imaged and uploaded into NeuroInfo® software (MBF Bioscience). All sections were manually reordered from rostral to caudal direction of the brain. The software's section detection parameters were adjusted to properly recognize the borders of each brain section. Sections were aligned, first using the software's "Most Accurate" alignment option, and then re-adjusted manually if necessary. The distance between each section (200 μm) was specified for the sections to be registered to a standardized 3-D mouse

brain atlas, using the "Section Registration" function of the software. For P30 mouse brains, the last version of the Mouse Allen Brain atlas was selected. Non-linear registration was run on each section to account for the slight distortions, such as imperfections from sectioning/mounting and/or asymmetry from the sectioning angle. In the "Cell Detection" function, parameters for cell size and distance from background were adjusted, although the use of H2B:tdTomato rabies, which are nuclear, greatly improves the detection specificity compared to other labeling. Neural Network with "pyramidal-p64-c1-v15.pbx" preset was used to automatically detect rabies infected nuclei in the red channel. Detection results were reviewed manually to correct for any detection mistakes (false positives or negatives). Final results were exported as a CSV file. Retrogradely labeled neurons were grouped into functional regions and normalized by the total of retrogradely labeled neurons per brain. Depending on the analysis, functional groups or subgroups of regions were defined as followed: local = S1 cortex respectively; contralateral = any neurons found in the non-injected contralateral side; other areas = all ipsilateral cortical areas except S1; primary = primary sensory areas: M1, S1, V1, A1; association = "other areas" - "primary areas"; First order thalamic nuclei: dLG, VB, LD, AV, VAL, MGB; Higher order = LP, PO, VM, MD, AM; Limbic = Pf, AD, CM; CL; PCN; Rhe/RH. Hierarchical functional organization of the thalamus, as first, higher order and Limbic populations reflect the genetic and functional identity of thalamic nuclei[21,22,24]. This organization of rabies retrogradely labeled thalamic neurons was previously used to identify thalamocortical pathway changes after sensory deprivation[97] and help us to distinguish whole thalamus versus subpopulation changes in the function of thalamocortical pathways.

Acknowledgements

Author contributions

G.P. and G.F. conceived the project, developed the methodology and wrote the manuscript. G.P., D.Dwivedi and D.Dumontier analyzed and interpreted the results. D.Dumontier and G.P. processed experimental data and designed the figures. G.P. designed the CRISPR and viral strategies/constructs. D.Dwivedi performed electrophysiological experiments and analysis. D.Dumontier recorded intrinsic properties from DREADD experiments and performed the corresponding analysis. G.P. analyzed scRNAseq datasets. A.MC.M and M.S. established and performed smFISH, respectively. S.Liebman. and D.Dumontier performed DREADD-dependent cell death experiments. D.J. quantified cell density and was blind to the experiments. G.P., D.Dwivedi, S.Liebman., M.S. and D.Dumontier performed stereotactic injections. G.P. performed the synaptic density experiments and analysis. Q.X. cloned and produced AAVs. Y.Q. completed the automated monosynaptic retrograde labeling analysis. M.S, G.P. and Y.Q. collected MoSeq recordings. S. Lin. and B.D. processed, analyzed and interpret the MoSeq behavioral experiments. B.D. helped writing the manuscript.

Declaration of interests

Gord Fishell is a founder of Regel Therapeutics, which has no competing interests with the present manuscript.

References

1. Wamsley, B., and Fishell, G. (2017). Genetic and activity-dependent mechanisms underlying interneuron diversity. Nat Rev Neurosci *18*, 299–309. 10.1038/nrn.2017.30.

2. Faust, T.E., Gunner, G., and Schafer, D.P. (2021). Mechanisms governing activity-dependent synaptic pruning in the developing mammalian CNS. Nat Rev Neurosci *22*, 657–673. 10.1038/s41583-021-00507-y.

3. Cossart, R., and Garel, S. (2022). Step by step: cells with multiple functions in cortical circuit assembly. Nat Rev Neurosci, 1–16. 10.1038/s41583-022-00585-6.

4. Porter, J.T., Johnson, C.K., and Agmon, A. (2001). Diverse Types of Interneurons Generate Thalamus-Evoked Feedforward Inhibition in the Mouse Barrel Cortex. J. Neurosci. *21*, 2699–2710. 10.1523/JNEUROSCI.21-08-02699.2001.

5. Cruikshank, S.J., Urabe, H., Nurmikko, A.V., and Connors, B.W. (2010). Pathway-Specific Feedforward Circuits between Thalamus and Neocortex Revealed by Selective Optical Stimulation of Axons. Neuron *65*, 230–245. 10.1016/j.neuron.2009.12.025.

6. Yu, J., Hu, H., Agmon, A., and Svoboda, K. (2019). Recruitment of GABAergic Interneurons in the Barrel Cortex during Active Tactile Behavior. Neuron *104*, 412-427.e4. 10.1016/j.neuron.2019.07.027.

7. Isaac, J.T.R., Crair, M.C., Nicoll, R.A., and Malenka, R.C. (1997). Silent Synapses during Development of Thalamocortical Inputs. Neuron *18*, 269–280. 10.1016/S0896-6273(00)80267-6.

8. Vardalaki, D., Chung, K., and Harnett, M.T. (2022). Filopodia are a structural substrate for silent synapses in adult neocortex. Nature *612*, 323–327. 10.1038/s41586-022-05483-6.

9. Daw, M.I., Ashby, M.C., and Isaac, J.T.R. (2007). Coordinated developmental recruitment of latent fast spiking interneurons in layer IV barrel cortex. Nat Neurosci *10*, 453–461. 10.1038/nn1866.

10. Katz, L.C., and Shatz, C.J. (1996). Synaptic Activity and the Construction of Cortical Circuits. Science *274*, 1133–1138. 10.1126/science.274.5290.1133.

11. Morris, R.G.M. (1999). D.O. Hebb: The Organization of Behavior, Wiley: New York; 1949. Brain Research Bulletin *50*, 437. 10.1016/S0361-9230(99)00182-3.

12. Feldman, D.E., Nicoll, R.A., and Malenka, R.C. (1999). Synaptic plasticity at thalamocortical synapses in developing rat somatosensory cortex: LTP, LTD, and silent synapses. Journal of Neurobiology *41*, 92–101. 10.1002/(SICI)1097-4695(199910)41:1<92::AID-NEU12>3.0.CO;2-U.

13. Turrigiano, G.G., and Nelson, S.B. (2004). Homeostatic plasticity in the developing nervous system. Nat Rev Neurosci *5*, 97–107. 10.1038/nrn1327.

14. Han, E.B., and Stevens, C.F. (2009). Development regulates a switch between post- and presynaptic strengthening in response to activity deprivation. Proceedings of the National Academy of Sciences *106*, 10817–10822. 10.1073/pnas.0903603106.

15. Butts, D., and Kanold, P. (2010). The Applicability of Spike Time Dependent Plasticity to Development. Frontiers in Synaptic Neuroscience *2*.

16. Wen, W., and Turrigiano, G.G. (2021). Developmental Regulation of Homeostatic Plasticity in Mouse Primary Visual Cortex. J. Neurosci. *41*, 9891–9905. 10.1523/JNEUROSCI.1200-21.2021.

17. Marques-Smith, A., Lyngholm, D., Kaufmann, A.-K., Stacey, J.A., Hoerder-Suabedissen, A., Becker, E.B.E., Wilson, M.C., Molnár, Z., and Butt, S.J.B. (2016). A Transient Translaminar GABAergic Interneuron Circuit Connects Thalamocortical Recipient Layers in Neonatal Somatosensory Cortex. Neuron *89*, 536–549. 10.1016/j.neuron.2016.01.015.

18. Tuncdemir, S.N., Wamsley, B., Stam, F.J., Osakada, F., Goulding, M., Callaway, E.M., Rudy, B., and Fishell, G. (2016). Early Somatostatin Interneuron Connectivity Mediates the Maturation of Deep Layer Cortical Circuits. Neuron *89*, 521–535. 10.1016/j.neuron.2015.11.020.

19. Picardo, M.A., Guigue, P., Bonifazi, P., Batista-Brito, R., Allene, C., Ribas, A., Fishell, G., Baude, A., and Cossart, R. (2011). Pioneer GABA cells comprise a subpopulation of hub neurons in the developing hippocampus. Neuron *71*, 695–709. 10.1016/j.neuron.2011.06.018.

20. Foeller, E., and Feldman, D.E. (2004). Synaptic basis for developmental plasticity in somatosensory cortex. Current Opinion in Neurobiology *14*, 89–95. 10.1016/j.conb.2004.01.011.

21. Clascá, F., Rubio-Garrido, P., and Jabaudon, D. (2012). Unveiling the diversity of thalamocortical neuron subtypes. European Journal of Neuroscience *35*, 1524–1532. 10.1111/j.1460-9568.2012.08033.x.

22. Frangeul, L., Pouchelon, G., Telley, L., Lefort, S., Luscher, C., and Jabaudon, D. (2016). A cross-modal genetic framework for the development and plasticity of sensory pathways. Nature *538*, 96–98. 10.1038/nature19770.

23. Halassa, M.M., and Sherman, S.M. (2019). Thalamocortical Circuit Motifs: A General Framework. Neuron *103*, 762–770. 10.1016/j.neuron.2019.06.005.

24. Phillips, J.W., Schulmann, A., Hara, E., Winnubst, J., Liu, C., Valakh, V., Wang, L., Shields, B.C., Korff, W., Chandrashekar, J., et al. (2019). A repeated molecular architecture across thalamic pathways. Nat Neurosci *22*, 1925–1935. 10.1038/s41593-019-0483-3.

25. Williams, L.E., and Holtmaat, A. (2019). Higher-Order Thalamocortical Inputs Gate Synaptic Long-Term Potentiation via Disinhibition. Neuron *101*, 91-102.e4. 10.1016/j.neuron.2018.10.049.

26. Pouchelon, G., Gambino, F., Bellone, C., Telley, L., Vitali, I., Lüscher, C., Holtmaat, A., and Jabaudon, D. (2014). Modality-specific thalamocortical inputs instruct the identity of postsynaptic L4 neurons. Nature *511*, 471–474. 10.1038/nature13390.

27. Li, H., Fertuzinhos, S., Mohns, E., Hnasko, T.S., Verhage, M., Edwards, R., Sestan, N., and Crair, M.C. (2013). Laminar and Columnar Development of Barrel Cortex Relies on Thalamocortical Neurotransmission. Neuron *79*, 970–986. 10.1016/j.neuron.2013.06.043.

28. Sermet, B.S., Truschow, P., Feyerabend, M., Mayrhofer, J.M., Oram, T.B., Yizhar, O., Staiger, J.F., and Petersen, C.C. (2019). Pathway-, layer- and cell-type-specific thalamic input to mouse barrel cortex. eLife *8*, e52665. 10.7554/eLife.52665.

29. Audette, N.J., Urban-Ciecko, J., Matsushita, M., and Barth, A.L. (2018). POm Thalamocortical Input Drives Layer-Specific Microcircuits in Somatosensory Cortex. Cerebral Cortex *28*, 1312–1328. 10.1093/cercor/bhx044.

30. Bureau, I., Paul, F. von S., and Svoboda, K. (2006). Interdigitated Paralemniscal and Lemniscal Pathways in the Mouse Barrel Cortex. PLOS Biology *4*, e382. 10.1371/journal.pbio.0040382.

31. Wimmer, V.C., Bruno, R.M., de Kock, C.P.J., Kuner, T., and Sakmann, B. (2010). Dimensions of a Projection Column and Architecture of VPM and POm Axons in Rat Vibrissal Cortex. Cerebral Cortex *20*, 2265–2276. 10.1093/cercor/bhq068.

32. Graziano, A., Liu, X.-B., Murray, K.D., and Jones, E.G. (2008). Vesicular glutamate transporters define two sets of glutamatergic afferents to the somatosensory thalamus and two thalamocortical projections in the mouse. Journal of Comparative Neurology *507*, 1258–1276. 10.1002/cne.21592.

33. Zhuang, J., Larsen, R.S., Takasaki, K.T., Ouellette, N.D., Daigle, T.L., Tasic, B., Waters, J., Zeng, H., and Reid, R.C. (2020). The spatial structure of feedforward information in mouse primary visual cortex. 2019.12.24.888156. 10.1101/2019.12.24.888156.

34. Ibrahim, L.A., Huang, S., Fernandez-Otero, M., Sherer, M., Qiu, Y., Vemuri, S., Xu, Q., Machold, R., Pouchelon, G., Rudy, B., et al. (2021). Bottom-up inputs are required for establishment of top-down connectivity onto cortical layer 1 neurogliaform cells. Neuron *109*, 3473-3485.e5. 10.1016/j.neuron.2021.08.004.

35. Taniguchi, H., He, M., Wu, P., Kim, S., Paik, R., Sugino, K., Kvitsani, D., Fu, Y., Lu, J., Lin, Y., et al. (2011). A Resource of Cre Driver Lines for Genetic Targeting of GABAergic Neurons in Cerebral Cortex. Neuron *71*, 995–1013. 10.1016/j.neuron.2011.07.026.

36. Murakami, T., Matsui, T., Uemura, M., and Ohki, K. (2022). Modular strategy for development of the hierarchical visual network in mice. Nature *608*, 578–585. 10.1038/s41586-022-05045-w.

37. Vasquez-Lopez, S.A., Weissenberger, Y., Lohse, M., Keating, P., King, A.J., and Dahmen, J.C. (2017). Thalamic input to auditory cortex is locally heterogeneous but globally tonotopic. eLife *6*, e25141. 10.7554/eLife.25141.

38. Antón-Bolaños, N., Sempere-Ferràndez, A., Guillamón-Vivancos, T., Martini, F.J., Pérez-Saiz, L., Gezelius, H., Filipchuk, A., Valdeolmillos, M., and López-Bendito, G. (2019). Prenatal activity from thalamic neurons governs the emergence of functional cortical maps in mice. Science *364*, 987–990. 10.1126/science.aav7617.

39. Narboux-Nême, N., Evrard, A., Ferezou, I., Erzurumlu, R.S., Kaeser, P.S., Lainé, J., Rossier, J., Ropert, N., Südhof, T.C., and Gaspar, P. (2012). Neurotransmitter Release at the Thalamocortical Synapse Instructs Barrel Formation But Not Axon Patterning in the Somatosensory Cortex. J. Neurosci. *32*, 6183–6196. 10.1523/JNEUROSCI.0343-12.2012.

40. Sherman, S.M. (2001). Tonic and burst firing: dual modes of thalamocortical relay. Trends in Neurosciences *24*, 122–126. 10.1016/S0166-2236(00)01714-8.

41. Yu, C., Derdikman, D., Haidarliu, S., and Ahissar, E. (2006). Parallel Thalamic Pathways for Whisking and Touch Signals in the Rat. PLOS Biology *4*, e124. 10.1371/journal.pbio.0040124.

42. Chou, S.-J., Babot, Z., Leingärtner, A., Studer, M., Nakagawa, Y., and O'Leary, D.D.M. (2013). Geniculocortical Input Drives Genetic Distinctions Between Primary and Higher-Order Visual Areas. Science *340*, 1239–1242. 10.1126/science.1232806.

43. Armbruster, B.N., Li, X., Pausch, M.H., Herlitze, S., and Roth, B.L. (2007). Evolving the lock to fit the key to create a family of G protein-coupled receptors potently activated by an inert ligand. Proceedings of the National Academy of Sciences *104*, 5163–5168. 10.1073/pnas.0700293104.

44. Urban, D.J., and Roth, B.L. (2015). DREADDs (Designer Receptors Exclusively Activated by Designer Drugs): Chemogenetic Tools with Therapeutic Utility. Annual Review of Pharmacology and Toxicology *55*, 399–417. 10.1146/annurev-pharmtox-010814-124803.

45. Wong, F.K., Bercsenyi, K., Sreenivasan, V., Portalés, A., Fernández-Otero, M., and Marín, O. (2018). Pyramidal cell regulation of interneuron survival sculpts cortical networks. Nature *557*, 668–673. 10.1038/s41586-018-0139-6.

46. Devienne, G., Picaud, S., Cohen, I., Piquet, J., Tricoire, L., Testa, D., Di Nardo, A.A., Rossier, J., Cauli, B., and Lambolez, B. (2021). Regulation of Perineuronal Nets in the Adult Cortex by the Activity of the Cortical Network. J Neurosci *41*, 5779–5790. 10.1523/JNEUROSCI.0434-21.2021.

47. De Marco García, N.V., Karayannis, T., and Fishell, G. (2011). Neuronal activity is required for the development of specific cortical interneuron subtypes. Nature *472*, 351–355. 10.1038/nature09865.

48. Priya, R., Paredes, M.F., Karayannis, T., Yusuf, N., Liu, X., Jaglin, X., Graef, I., Alvarez-Buylla, A., and Fishell, G. (2018). Activity Regulates Cell Death within Cortical Interneurons through a Calcineurin-Dependent Mechanism. Cell Reports *22*, 1695–1709. 10.1016/j.celrep.2018.01.007.

49. Karayannis, T., De Marco Garcia, N., and Fishell, G. (2012). Functional adaptation of cortical interneurons to attenuated activity is subtype-specific. Frontiers in Neural Circuits *6*.

50. Vitali, I., Fièvre, S., Telley, L., Oberst, P., Bariselli, S., Frangeul, L., Baumann, N., McMahon, J.J., Klingler, E., Bocchi, R., et al. (2018). Progenitor Hyperpolarization Regulates the Sequential Generation of Neuronal Subtypes in the Developing Neocortex. Cell *174*, 1264-1276.e15. 10.1016/j.cell.2018.06.036.

51. Martini, F.J., Guillamón-Vivancos, T., Moreno-Juan, V., Valdeolmillos, M., and López-Bendito, G. (2021). Spontaneous activity in developing thalamic and cortical sensory networks. Neuron *109*, 2519–2534. 10.1016/j.neuron.2021.06.026.

52. Ibrahim, L.A., Wamsley, B., Alghamdi, N., Yusuf, N., Sevier, E., Hairston, A., Sherer, M., Jaglin, X.H., Xu, Q., Guo, L., et al. (2023). Nova proteins direct synaptic integration of somatostatin interneurons through activity-dependent alternative splicing. eLife *12*, e86842. 10.7554/eLife.86842.

53. Allaway, K.C., Gabitto, M.I., Wapinski, O., Saldi, G., Wang, C.-Y., Bandler, R.C., Wu, S.J., Bonneau, R., and Fishell, G. (2021). Genetic and epigenetic coordination of cortical interneuron development. Nature *597*, 693–697. 10.1038/s41586-021-03933-1.

54. Mayer, C., Hafemeister, C., Bandler, R.C., Machold, R., Batista Brito, R., Jaglin, X., Allaway, K., Butler, A., Fishell, G., and Satija, R. (2018). Developmental diversification of cortical inhibitory interneurons. Nature *555*, 457–462. 10.1038/nature25999.

55. Stuart, T., Butler, A., Hoffman, P., Hafemeister, C., Papalexi, E., Mauck, W.M., Hao, Y., Stoeckius, M., Smibert, P., and Satija, R. (2019). Comprehensive Integration of Single-Cell Data. Cell *177*, 1888-1902.e21. 10.1016/j.cell.2019.05.031.

56. Satija, R., Farrell, J.A., Gennert, D., Schier, A.F., and Regev, A. (2015). Spatial reconstruction of single-cell gene expression data. Nat Biotechnol *33*, 495–502. 10.1038/nbt.3192.

57. Wu, S.J., Sevier, E., Dwivedi, D., Saldi, G.-A., Hairston, A., Yu, S., Abbott, L., Choi, D.H., Sherer, M., Qiu, Y., et al. (2023). Cortical somatostatin interneuron subtypes form cell-type-specific circuits. Neuron. 10.1016/j.neuron.2023.05.032.

58. Baude, A., Nusser, Z., Roberts, J.D.B., Mulvihill, E., Jeffrey McIlhinney, R.A., and Somogyi, P. (1993). The metabotropic glutamate receptor (mGluRIα) is concentrated at perisynaptic membrane of neuronal subpopulations as detected by immunogold reaction. Neuron *11*, 771–787. 10.1016/0896-6273(93)90086-7.

59. McBain, C.J., DiChiara, T.J., and Kauer, J.A. (1994). Activation of metabotropic glutamate receptors differentially affects two classes of hippocampal interneurons and potentiates excitatory synaptic transmission. J. Neurosci. *14*, 4433–4445. 10.1523/JNEUROSCI.14-07-04433.1994.

60. Lapointe, V., Morin, F., Ratté, S., Croce, A., Conquet, F., and Lacaille, J.-C. (2004). Synapse-specific mGluR1-dependent long-term potentiation in interneurones regulates mouse hippocampal inhibition. The Journal of Physiology *555*, 125–135. 10.1113/jphysiol.2003.053603.

61. Maksymetz, J., Byun, N.E., Luessen, D.J., Li, B., Barry, R.L., Gore, J.C., Niswender, C.M., Lindsley, C.W., Joffe, M.E., and Conn, P.J. (2021). mGlu1 potentiation enhances prelimbic somatostatin interneuron activity to rescue schizophrenia-like physiological and cognitive deficits. Cell Reports *37*, 109950. 10.1016/j.celrep.2021.109950.

62. Lüscher, C., and Huber, K.M. (2010). Group 1 mGluR-dependent synaptic long-term depression (mGluR-LTD): mechanisms and implications for circuitry & disease. Neuron *65*, 445–459. 10.1016/j.neuron.2010.01.016.

63. Narushima, M., Uchigashima, M., Yagasaki, Y., Harada, T., Nagumo, Y., Uesaka, N., Hashimoto, K., Aiba, A., Watanabe, M., Miyata, M., et al. (2016). The Metabotropic Glutamate Receptor Subtype 1 Mediates Experience-Dependent Maintenance of Mature Synaptic Connectivity in the Visual Thalamus. Neuron *91*, 1097–1109. 10.1016/j.neuron.2016.07.035.

64. Micheva, K.D., and Beaulieu, C. (1996). Quantitative aspects of synaptogenesis in the rat barrel field cortex with special reference to GABA circuitry. Journal of Comparative Neurology *373*, 340–354. 10.1002/(SICI)1096-9861(19960923)373:3<340::AID-CNE3>3.0.CO;2-2.

65. Markowitz, J.E., Gillis, W.F., Beron, C.C., Neufeld, S.Q., Robertson, K., Bhagat, N.D., Peterson, R.E., Peterson, E., Hyun, M., Linderman, S.W., et al. (2018). The Striatum Organizes 3D Behavior via Moment-to-Moment Action Selection. Cell *174*, 44-58.e17. 10.1016/j.cell.2018.04.019.

66. Wiltschko, A.B., Johnson, M.J., Iurilli, G., Peterson, R.E., Katon, J.M., Pashkovski, S.L., Abraira, V.E., Adams, R.P., and Datta, S.R. (2015). Mapping Sub-Second Structure in Mouse Behavior. Neuron *88*, 1121–1135. 10.1016/j.neuron.2015.11.031.

67. Rong, R., Ahn, J.-Y., Huang, H., Nagata, E., Kalman, D., Kapp, J.A., Tu, J., Worley, P.F., Snyder, S.H., and Ye, K. (2003). PI3 kinase enhancer–Homer complex couples mGluRI to PI3 kinase, preventing neuronal apoptosis. Nat Neurosci *6*, 1153–1161. 10.1038/nn1134.

68. Wang, H., and Zhuo, M. (2012). Group I Metabotropic Glutamate Receptor-Mediated Gene Transcription and Implications for Synaptic Plasticity and Diseases. Front Pharmacol *3*, 189. 10.3389/fphar.2012.00189.

69. Bear, M.F., Huber, K.M., and Warren, S.T. (2004). The mGluR theory of fragile X mental retardation. Trends in Neurosciences *27*, 370–377. 10.1016/j.tins.2004.04.009.

70. Uesaka, N., Uchigashima, M., Mikuni, T., Nakazawa, T., Nakao, H., Hirai, H., Aiba, A., Watanabe, M., and Kano, M. (2014). Retrograde semaphorin signaling regulates synapse elimination in the developing mouse brain. Science *344*, 1020–1023. 10.1126/science.1252514.

71. Kreibich, T.A., Chalasani, S.H., and Raper, J.A. (2004). The Neurotransmitter Glutamate Reduces Axonal Responsiveness to Multiple Repellents through the Activation of Metabotropic Glutamate Receptor 1. J. Neurosci. *24*, 7085–7095. 10.1523/JNEUROSCI.0349-04.2004.

72. Giger, R.J., Pasterkamp, R.J., Holtmaat, A.J.G.D., and Verhaagen, J. (1998). Chapter 12 Semaphorin III: Role in neuronal development and structural plasticity. In Progress in Brain Research Neuronal Degeneration and Regeneration: From Basic Mechanisms to Prospects for Therapy., J. A. Callow, ed. (Elsevier), pp. 133–149. 10.1016/S0079-6123(08)64013-3.

73. Shelly, M., Cancedda, L., Lim, B.K., Popescu, A.T., Cheng, P., Gao, H., and Poo, M. (2011). Semaphorin3A Regulates Neuronal Polarization by Suppressing Axon Formation and Promoting Dendrite Growth. Neuron *71*, 433–446. 10.1016/j.neuron.2011.06.041.

74. Wang, N., Dhumale, P., Chiang, J., and Püschel, A.W. (2018). The Sema3A receptor Plexin-A1 suppresses supernumerary axons through Rap1 GTPases. Sci Rep *8*, 15647. 10.1038/s41598-018-34092-5.

75. Lein, E.S., Hawrylycz, M.J., Ao, N., Ayres, M., Bensinger, A., Bernard, A., Boe, A.F., Boguski, M.S., Brockway, K.S., Byrnes, E.J., et al. (2007). Genome-wide atlas of gene expression in the adult mouse brain. Nature *445*, 168–176. 10.1038/nature05453.

76. Hensch, T.K. (2005). Critical period plasticity in local cortical circuits. Nat Rev Neurosci *6*, 877–888. 10.1038/nrn1787.

77. Erzurumlu, R.S., and Gaspar, P. (2020). How the Barrel Cortex Became a Working Model for Developmental Plasticity: A Historical Perspective. J Neurosci *40*, 6460–6473. 10.1523/JNEUROSCI.0582-20.2020.

78. Morishita, H., Miwa, J.M., Heintz, N., and Hensch, T.K. (2010). Lynx1, a Cholinergic Brake, Limits Plasticity in Adult Visual Cortex. Science *330*, 1238–1240. 10.1126/science.1195320.

79. Sadahiro, M., Demars, M.P., Burman, P., Yevoo, P., Zimmer, A., and Morishita, H. (2020). Activation of Somatostatin Interneurons by Nicotinic Modulator Lypd6 Enhances Plasticity and Functional Recovery in the Adult Mouse Visual Cortex. J Neurosci *40*, 5214–5227. 10.1523/JNEUROSCI.1373-19.2020.

80. Kastli, R., Vighagen, R., van der Bourg, A., Argunsah, A.Ö., Iqbal, A., Voigt, F.F., Kirschenbaum, D., Aguzzi, A., Helmchen, F., and Karayannis, T. (2020). Developmental divergence of sensory stimulus representation in cortical interneurons. Nat Commun *11*, 5729. 10.1038/s41467-020-19427-z.

81. Dorskind, J.M., and Kolodkin, A.L. (2021). Revisiting and refining roles of neural guidance cues in circuit assembly. Current Opinion in Neurobiology *66*, 10–21. 10.1016/j.conb.2020.07.005.

82. Sidorov, M.S., Kaplan, E.S., Osterweil, E.K., Lindemann, L., and Bear, M.F. (2015). Metabotropic glutamate receptor signaling is required for NMDA receptor-dependent ocular dominance

plasticity and LTD in visual cortex. Proceedings of the National Academy of Sciences *112*, 12852–12857. 10.1073/pnas.1512878112.

83. Penzes, P., Cahill, M.E., Jones, K.A., VanLeeuwen, J.-E., and Woolfrey, K.M. (2011). Dendritic spine pathology in neuropsychiatric disorders. Nat Neurosci *14*, 285–293. 10.1038/nn.2741.

84. Nelson, S.B., and Valakh, V. (2015). Excitatory/Inhibitory Balance and Circuit Homeostasis in Autism Spectrum Disorders. Neuron *87*, 684–698. 10.1016/j.neuron.2015.07.033.

85. Hadders-Algra, M. (2022). Emerging signs of autism spectrum disorder in infancy: Putative neural substrate. Developmental Medicine & Child Neurology *64*, 1344–1350. 10.1111/dmcn.15333.

86. He, M., Tucciarone, J., Lee, S., Nigro, M.J., Kim, Y., Levine, J.M., Kelly, S.M., Krugikov, I., Wu, P., Chen, Y., et al. (2016). Strategies and Tools for Combinatorial Targeting of GABAergic Neurons in Mouse Cerebral Cortex. Neuron *91*, 1228–1243. 10.1016/j.neuron.2016.08.021.

87. Daigle, T.L., Madisen, L., Hage, T.A., Valley, M.T., Knoblich, U., Larsen, R.S., Takeno, M.M., Huang, L., Gu, H., Larsen, R., et al. (2018). A Suite of Transgenic Driver and Reporter Mouse Lines with Enhanced Brain-Cell-Type Targeting and Functionality. Cell *174*, 465-480.e22. 10.1016/j.cell.2018.06.035.

88. Platt, R.J., Chen, S., Zhou, Y., Yim, M.J., Swiech, L., Kempton, H.R., Dahlman, J.E., Parnas, O., Eisenhaure, T.M., Jovanovic, M., et al. (2014). CRISPR-Cas9 Knockin Mice for Genome Editing and Cancer Modeling. Cell *159*, 440–455. 10.1016/j.cell.2014.09.014.

89. Sousa, V.H., Miyoshi, G., Hjerling-Leffler, J., Karayannis, T., and Fishell, G. (2009). Characterization of Nkx6-2-Derived Neocortical Interneuron Lineages. Cerebral Cortex *19*, i1–i10. 10.1093/cercor/bhp038.

90. Hippenmeyer, S., Vrieseling, E., Sigrist, M., Portmann, T., Laengle, C., Ladle, D.R., and Arber, S. (2005). A Developmental Switch in the Response of DRG Neurons to ETS Transcription Factor Signaling. PLOS Biology *3*, e159. 10.1371/journal.pbio.0030159.

91. Pouchelon, G., Vergara, J., McMahon, J., Gorissen, B.L., Lin, J.D., Vormstein-Schneider, D., Niehaus, J.L., Burbridge, T.J., Wester, J.C., Sherer, M., et al. (2022). A versatile viral toolkit for functional discovery in the nervous system. Cell Reports Methods *2*, 100225. 10.1016/j.crmeth.2022.100225.

92. Marshel, J.H., Kim, Y.S., Machado, T.A., Quirin, S., Benson, B., Kadmon, J., Raja, C., Chibukhchyan, A., Ramakrishnan, C., Inoue, M., et al. (2019). Cortical layer–specific critical dynamics triggering perception. Science *365*, eaaw5202. 10.1126/science.aaw5202.

93. Chan, K.Y., Jang, M.J., Yoo, B.B., Greenbaum, A., Ravi, N., Wu, W.-L., Sánchez-Guardado, L., Lois, C., Mazmanian, S.K., Deverman, B.E., et al. (2017). Engineered AAVs for efficient noninvasive gene delivery to the central and peripheral nervous systems. Nat Neurosci *20*, 1172–1179. 10.1038/nn.4593.

94. Fenno, L.E., Mattis, J., Ramakrishnan, C., Hyun, M., Lee, S.Y., He, M., Tucciarone, J., Selimbeyoglu, A., Berndt, A., Grosenick, L., et al. (2014). Targeting cells with single vectors using multiple-feature Boolean logic. Nat Methods *11*, 763–772. 10.1038/nmeth.2996.

95. Schneeberger, M., Parolari, L., Das Banerjee, T., Bhave, V., Wang, P., Patel, B., Topilko, T., Wu, Z., Choi, C.H.J., Yu, X., et al. (2019). Regulation of Energy Expenditure by Brainstem GABA Neurons. Cell *178*, 672-685.e12. 10.1016/j.cell.2019.05.048.

96. Vormstein-Schneider, D., Lin, J.D., Pelkey, K.A., Chittajallu, R., Guo, B., Arias-Garcia, M.A., Allaway, K., Sakopoulos, S., Schneider, G., Stevenson, O., et al. (2020). Viral manipulation of functionally distinct interneurons in mice, non-human primates and humans. Nat Neurosci *23*, 1629–1636. 10.1038/s41593-020-0692-9.

97. Pouchelon, G., Dwivedi, D., Bollmann, Y., Agba, C.K., Xu, Q., Mirow, A.M.C., Kim, S., Qiu, Y., Sevier, E., Ritola, K.D., et al. (2021). The organization and development of cortical interneuron presynaptic circuits are area specific. Cell Reports *37*. 10.1016/j.celrep.2021.109993.

98. Labun, K., Montague, T.G., Krause, M., Torres Cleuren, Y.N., Tjeldnes, H., and Valen, E. (2019). CHOPCHOP v3: expanding the CRISPR web toolbox beyond genome editing. Nucleic Acids Research *47*, W171–W174. 10.1093/nar/gkz365.

99. Labun, K., Montague, T.G., Gagnon, J.A., Thyme, S.B., and Valen, E. (2016). CHOPCHOP v2: a web tool for the next generation of CRISPR genome engineering. Nucleic Acids Research *44*, W272–W276. 10.1093/nar/gkw398.

100. Loo, L., Simon, J.M., Xing, L., McCoy, E.S., Niehaus, J.K., Guo, J., Anton, E.S., and Zylka, M.J. (2019). Single-cell transcriptomic analysis of mouse neocortical development. Nat Commun *10*, 134. 10.1038/s41467-018-08079-9.

101. Virtanen, P., Gommers, R., Oliphant, T.E., Haberland, M., Reddy, T., Cournapeau, D., Burovski, E., Peterson, P., Weckesser, W., Bright, J., et al. (2020). SciPy 1.0: fundamental algorithms for scientific computing in Python. Nat Methods *17*, 261–272. 10.1038/s41592-019-0686-2.

102. Favuzzi, E., Marques-Smith, A., Deogracias, R., Winterflood, C.M., Sánchez-Aguilera, A., Mantoan, L., Maeso, P., Fernandes, C., Ewers, H., and Rico, B. (2017). Activity-Dependent Gating of Parvalbumin Interneuron Function by the Perineuronal Net Protein Brevican. Neuron *95*, 639-655.e10. 10.1016/j.neuron.2017.06.028.

103. Collins, D.P., Anastasiades, P.G., Marlin, J.J., and Carter, A.G. (2018). Reciprocal Circuits Linking the Prefrontal Cortex with Dorsal and Ventral Thalamic Nuclei. Neuron *98*, 366-379.e4. 10.1016/j.neuron.2018.03.024.

104. Hay, Y.A., Naudé, J., Faure, P., and Lambolez, B. (2019). Target Interneuron Preference in Thalamocortical Pathways Determines the Temporal Structure of Cortical Responses. Cerebral Cortex *29*, 2815–2831. 10.1093/cercor/bhy148.
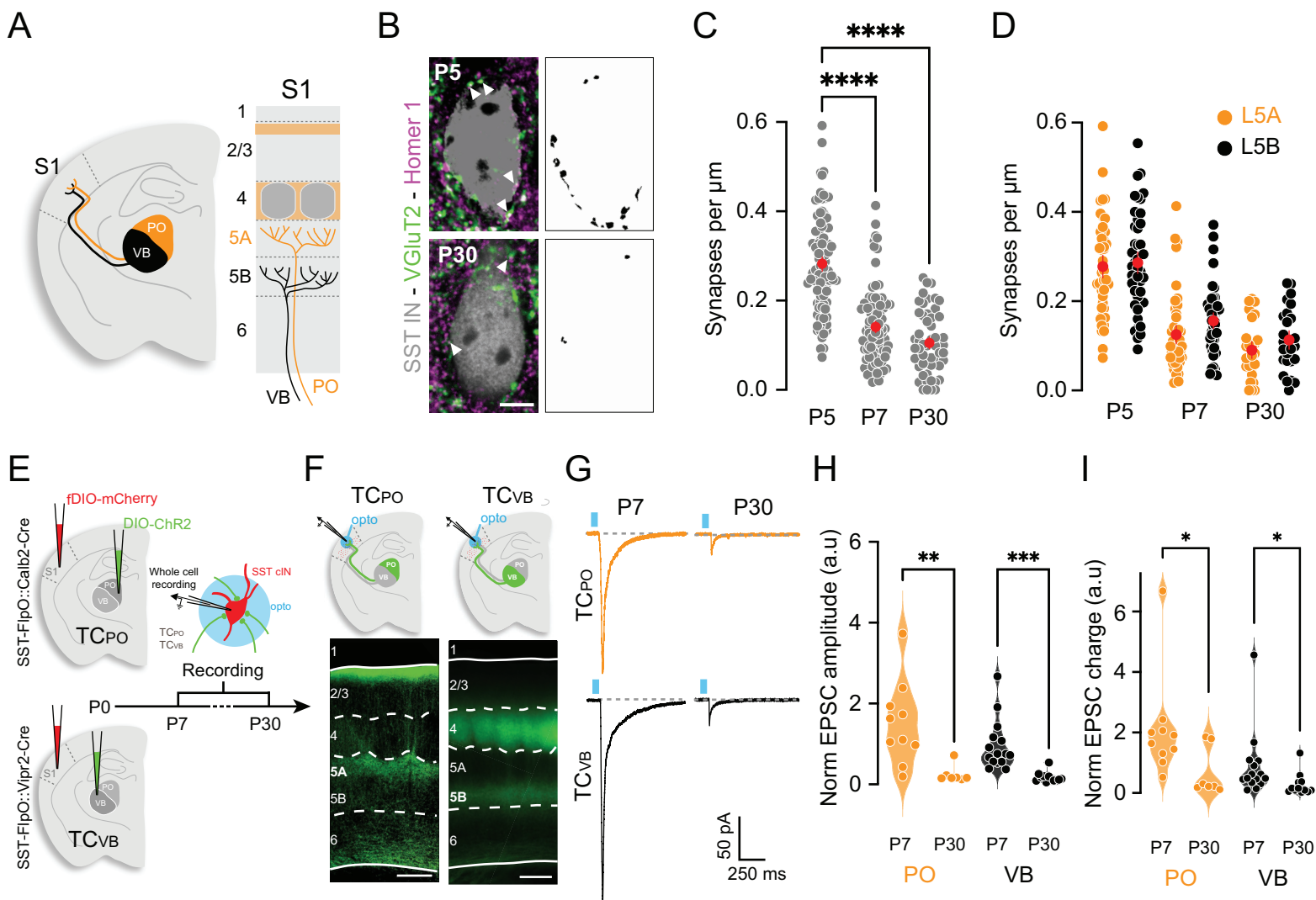
Figure 1. Transient TC connectivity onto SST cINs is input-independent

**Figure 1: Transient TC connectivity onto SST cINs is input-independent**

A) TC neurons from VB and PO primarily project to L5A and L5B of the cortex. B) Staining of VGluT2 (presynaptic) and Homer1 (postsynaptic) TC synapses onto SST cINs, labeled with SST-cre mouse line and fluorescent reporters. Masks of puncta colocalizations on the soma at P5 and P30 in L5. Scale bar 5μm. C) Quantification of VGluT2+, Homer1+ TC synapses onto SST cINs in L5. During development, the number of synapses onto SST soma is decreased. One-way ANOVA (p-value <0.0001), followed by Tukey's multiple comparison test (P5-P7 <0.0001; P5-P30 <0.0001; P7-P30 = 0.0716; P5 0.28±0.01 n=89 N=3, P7 0.14±0.009 n=87 N=3, P30 0.105±0.009 n=54 N=3). D) The same quantification was performed based on the localization of the SST cINs in L5A vs L5B, the PO and VB receiving layers, respectively. No significant difference in TC synapses number was detected between the layers at each age. One-way ANOVA E) AAV Cre-dependent DIO-ChRmine or -ChR2 controlled under Vipr2-Cre or CR-Cre mouse lines, targeting VB and PO respectively, and Flp-dependent fluorescence (fDIO) reporters under the control of SST-FlpO allows for specific recording of SST cIN responses to TC$_{VB}$ or TC$_{PO}$ inputs. AAVs were injected at P0 and responses were recorded at P6-P7 for developmental time point and at P28-P32 for adult time point. F) TC projections from VB and PO AAV-opsin infection at P30. Scale bar 200μm. G) Example traces of SST cIN responses at P7 and P30 upon light stimulation of TC$_{VB}$ and TC$_{PO}$ projections. H) The peak amplitude of EPSCs (excitatory postsynaptic currents) normalized to neighboring pyramidal cells in L5, decreases over development, independently from the origin of the activated TC inputs. Kruskal-Wallis test (p-value <0.0001), followed by Dunn's multiple comparison tests (p-value for VB P7-P30=0.0003, for PO P7-P30=0.0068; VB P7 0.97±0.16 n=15 N=4, VB P30 0.17±0.38 n=12 N= 3, PO P7 1.51±0.32 n=10 N=2, PO 0.24±0.08 P30 n=7, N=2). I) EPSC charges normalized to neighboring pyramidal cells in L5 decrease over development, independently from the origin of the activated TC inputs. Kruskal-Wallis test (p-value=0.0001) followed by Dunn's multiple comparison tests (p-values for VB P7-P30=0.0266, PO P7-P30=0.0189; VB P7 0.89±0.28 n=15 N=4, VB P30 0.28±0.11 n=12 N= 3, PO P7 2.10±0.54 n=10 N=2, PO P30 0.67±0.30 n=7, N=2).
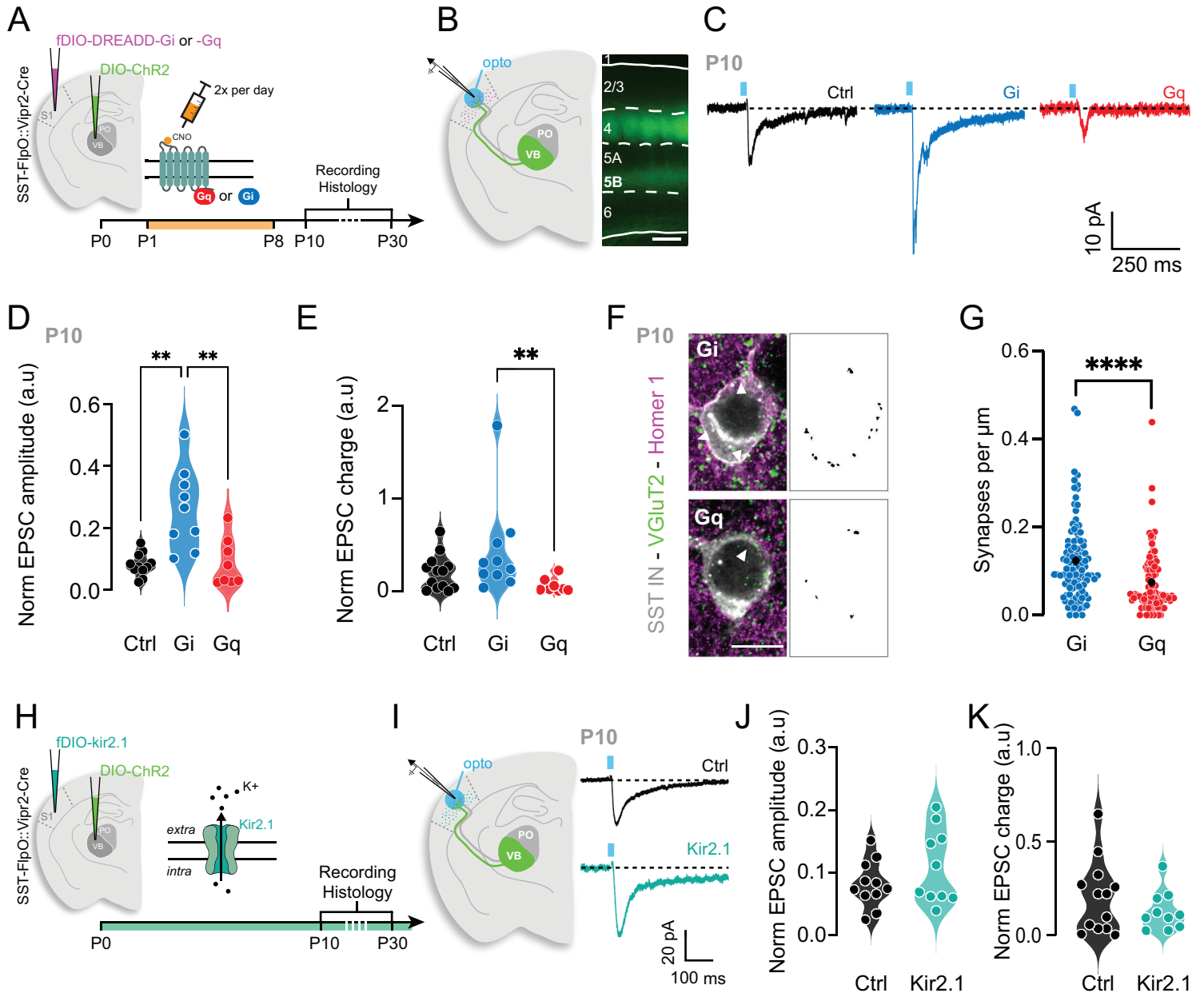
Figure 2. Postsynaptic metabotropic signaling in SST cINs regulates the maturation of transient TC inputs.

Figure 2: Postsynaptic metabotropic signaling in SST cINs regulates the maturation of transient TC inputs

A) Designer Receptors Exclusively Activated by Designer Drugs (DREADD)-based chemogenetic tools used to test activity-dependent maturation of TC inputs onto SST cINs. DREADD coupled with Gi inhibits cINs, while DREADD coupled with Gq activates neurons upon delivery of the designer drug Clozapine-N-Oxide (CNO). 12-24hrs following local AAV injections in the cortex and in the thalamus at postnatal day 0 (P0), DREADD-Gi or -Gq are chronically activated during TC connection to SST cIN maturation, with intraperitoneal (i.p.) injection of CNO twice a day until P8. Animals are sacrificed for recording or synaptic analysis after maturation occurs at P10 and P30. B) AAV-driven Cre-dependent ChR2 expression in VB is controlled by Vipr2-Cre mouse line at P10. C) Example response traces from control SST cINs and SST cINs chronically-inhibited with Gi or -activated with Gq. D) At P10, normalized EPSCs peak amplitudes are significantly increased after Gi expression compared to Control or Gq-expressing SST cINs. Kruskal-Wallis test (p-value=0.0017) followed by Dunn's multiple comparison test (p-values for Ctrl-Gi=0.0045, Gi-Gq=0.0077; Ctrl 1.29±0.24 n=11 N=3, Gi 1.50±0.75 n=9 N=3, Gq 0.08±0.02 n=8 N=3). E) At P10, normalized EPSC charge is significantly decreased between SST cIN expressing Gi and Gq. Kruskal-Wallis test (p-value=0.0129) followed by Dunn's multiple comparison tests (p-value for Gi-Gq=0.0095; Ctrl 0.20±0.05 n=11 N=3, Gi 0.43±0.16 n=9 N=3, Gq 0.07±0.03 n=8 N=3). F) VGluT2 (presynaptic) and Homer1 (postsynaptic) staining of TC synapses onto SST cINs and masks of puncta colocalization measured on the soma of Gi- and Gq-expressing SST cINs in L5. Scale bar: 10 μm. G) Quantification of VGluT2+/Homer1+ TC synapses onto SST cINs in L5 shows a decrease of the number of synapses onto SST cINs expressing Gq compared to SST cINs expressing Gi. Mann-Whitney test (p-value <0.0001, Gi 0.123±0.009 n=105 N=3, Gq 0.074±0.007 n=94 N=3). H) Potassium ionotropic channel Kir2.1 used to test inhibitory activity of SST cINs compared to metabotropic signaling on TC synaptic maturation. AAV-driven Cre-dependent ChR2 expression in VB is controlled by Vipr2-Cre mouse line. Flp-dependent Kir2.1 (fDIO) expression in SST cINs is controlled by SST-FlpO mouse line. J) Examples of responses from control and Kir2.1-expressing cINs upon VB fibers stimulation. K) Quantification of SST cIN responses, which do not show significant change in EPSC peak amplitudes and charges normalized to neighboring pyramidal cells between control and Kir2.1 expressing SST cINs in L5 at P10. Mann-Whitney test (Ctrl from Fig. 2D-E; Kir2.1 amplitude 0.11±0.02; charge 0.13±0.03 n=10 N=3).
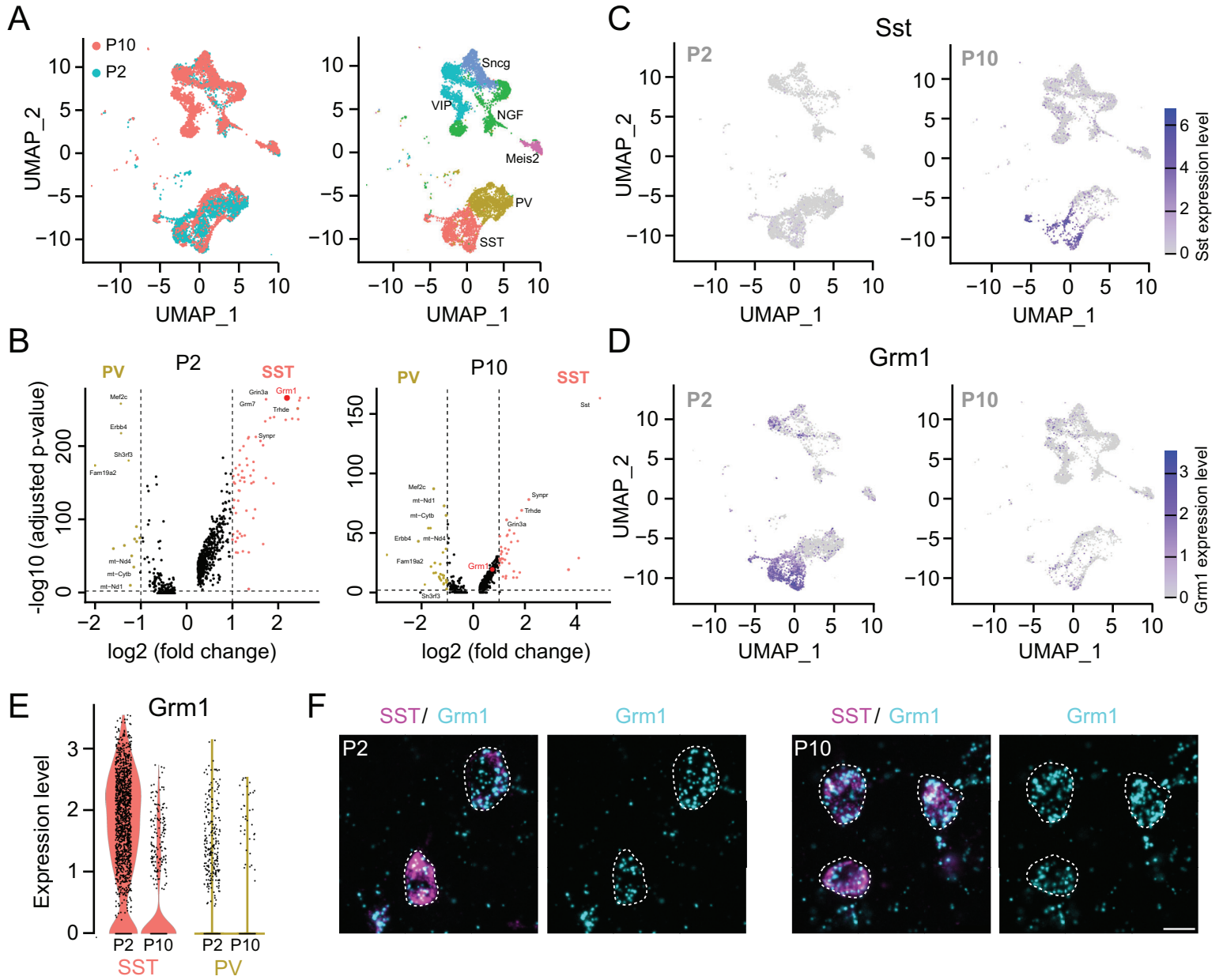
Figure 3. mGluR1 is highly expressed in SST cINs during development

Figure 3: mGluR1 is highly expressed in SST cINs during development

A) UMAP representation of the integration of P2 and P10 cortical GABAergic neurons scRNA-seq public databases[53,54] allowing for the identification of SST cINs at both stages. Left UMAP is color-coded by time-point, right UMAP is color-coded by major cIN classes based on the expression markers as previously described.[54,57] B) Differential gene expression between PV and SST cIN clusters using Seurat non-parametric Wilcoxon rank sum test. Volcano plot representing the average of the Fold Change (FC) and adjusted p-value of genes specifically expressed in PV and SST cIN clusters. At P2, Grm1 (blue) coding for mGluR1 is in one of the 3 highest significant genes in SST cINs and the top 3rd differentially expressed gene (Fold Change=4.53, adj. p-value=<9E-264). While still significant at P10 (adj. p-value=7.43E-20), the FC is only x1.64. C) & D) UMAP representation of scRNAseq P2 and P10 datasets with expression levels for Sst and Grm1 showing the reverse temporal dynamics in expression levels. E) Violin plots representing the level of Grm1 expression in cells from SST and PV cIN clusters at P2 and P10. F) smFISH of Grm1 combined with Sst immunostaining at P2 and P10, shows the high colocalization of Grm1 RNA molecules in SST cINs. Scale bar: 10 μm
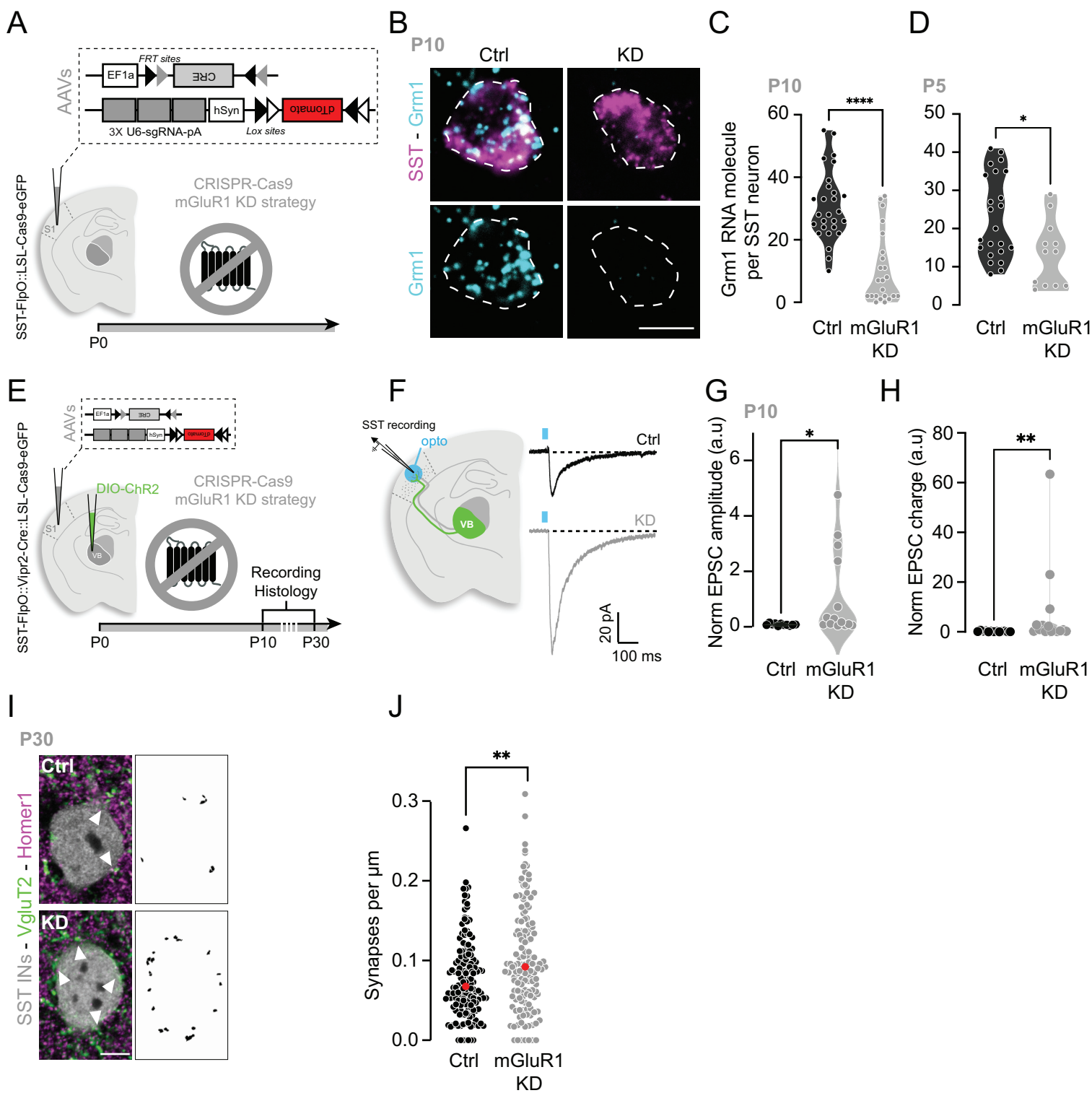
Figure 4. mGluR1 CRISPR-deleted SST cINs retain their strong developmental TC inputs

Figure 4: mGluR1 CRISPR-deleted SST cINs retain their strong developmental TC inputs
A) mGluR1 is a postsynaptic metabotropic receptor coupled to Gq protein activated by the presynaptic release of glutamate, similarly to Dreadd-Gq. Strategy for early deletion of mGluR1 in SST cINs specifically, using CRISPR/cas9 system: AAV-driven Flp-dependent Cre expression is driven by SST-FlpO mouse line and controls LSL-Cas9eGFP mouse line. 3x CRISPR single guide RNAs targeting mGluR1 are driven by an AAV expressing a Cre-dependent reporter. AAVs were injected in S1 at P0. B) Examples of Grm1 expression smFISH of Grm1 combined with Sst immunostaining at P10. Scale bar: 10 μm. C) & D) Quantification of particles number of Grm1 per SST cIN using smFISH, showing the major deletion of Grm1 expression in the mGluR1 CRISPR KD at P10 and P5. Student t-test at P10 (p-value <0.0001, Ctrl 30.89±2.17 n=27 N=2, KD 10.35±2.35 n=23 N=2) and at P5 (p-value=0.0117, Ctrl 23.09±2.29 n=23 N=2, KD 13.33±2.48 n=12 N=2). E) Experimental timeline: AAVs were injected at P0 in SST-FlpO:Vipr2-Cre:LSL-Cas9eGFP and analysis performed after transient connectivity maturation, at P10 and at P30. F) Recording of labeled control and CRISPR KD SST cINs upon VB projection stimulation in L5. Example response traces from control SST cINs labeled in response to VB fiber stimulation at P10. G) EPSCs peak amplitudes of SST cINs normalized to the peak amplitude of neighboring pyramidal cells are significantly increased in SST cINs deleted for mGluR1 compared to control cINs at P10. Mann-Whitney test (p-value=0.033; Ctrl from Fig. 2C 0.08±0.01; mGluR1 KD 1.09±0.42 n=15 N=4). H) Normalized EPSC charges of SST cINs deleted for mGluR1 are significantly increased compared to control SST cINs. Mann-Whitney test (p-value=0.0052; Ctrl Fig. 2D 0.20±0.05; mGluR1 KD 7.10±4.31 n=15 N=4). I) VGluT2 (presynaptic) and Homer1 (postsynaptic) staining of TC synapses onto SST cINs and masks of puncta colocalization measured on the soma of control SST cINs and SST cINs, CRISPR-deleted for mGluR1 in L5 at P30. Scale bar: 5 μm. J) Quantification of VGluT2+/Homer1+ TC synapses onto SST cINs in L5 shows an increase of the number of synapses onto SST cINs CRISPR-deleted for mGluR1 compared to control SST cINs. Mann-Whitney test (p-value=0.0014; Ctrl 0.077±0.004 n=152 N=4; mGluR1 KD 0.101±0.005 n=140 N=4).

43

Figure 5. The persistence of developmental TC inputs disrupts exploratory behavior at adulthood

Figure 5: The persistence of developmental TC inputs disrupts exploratory behavior at adulthood.

A) Strategy for early deletion of mGluR1 in SST cINs specifically, using CRISPR/cas9 system: AAV-driven Flp-dependent Cre expression is driven by SST-FlpO mouse line and controls LSL-Cas9eGFP mouse line. 3x CRISPR single guide RNAs targeting mGluR1 are driven by an AAV expressing a Cre-dependent reporter. AAVs were injected bilaterally in S1 at P0. Animals were recorded around P60 for MoSeq. B) Example of the bilateral S1 expression of gRNA-reporter expression after recording. C) MoSeq analysis. Examples of behavioral motifs, so-called syllables analyzed with MoSeq. D) & E) Syllable for Ctrl and mGluR1 KD female and male mice sorted by usage. The differences between two groups are tested Chi-square test on the unnormalized syllable usages (p-value<0.01). F) Linear Discriminant Analysis (LDA) plot shows that Ctrl and mGluR1 mice are separated by the syllable ensemble (males and females combined). 19 unique syllables were revealed from 76 iterations of LDA and are indicated in (E) & (D) by a red star. They include 8 forms of rear up, 3 forms of mid rear, 6 forms of groom, 1 scrunch and 1 dart syllables, reflective of mouse exploratory behavior using sensory cues. G) Confusion matrices for classification accuracy of a linear classifier trained on the 10 most frequently used syllables identified from LDA iterations by sex. The use of these syllables alone could predict Ctrl or KD mice. The classifier yields to 0.69 and 0.84 accuracy across cross-validation for females and males, respectively (top/bottom). Labels per-mouse are shuffled for control (right).
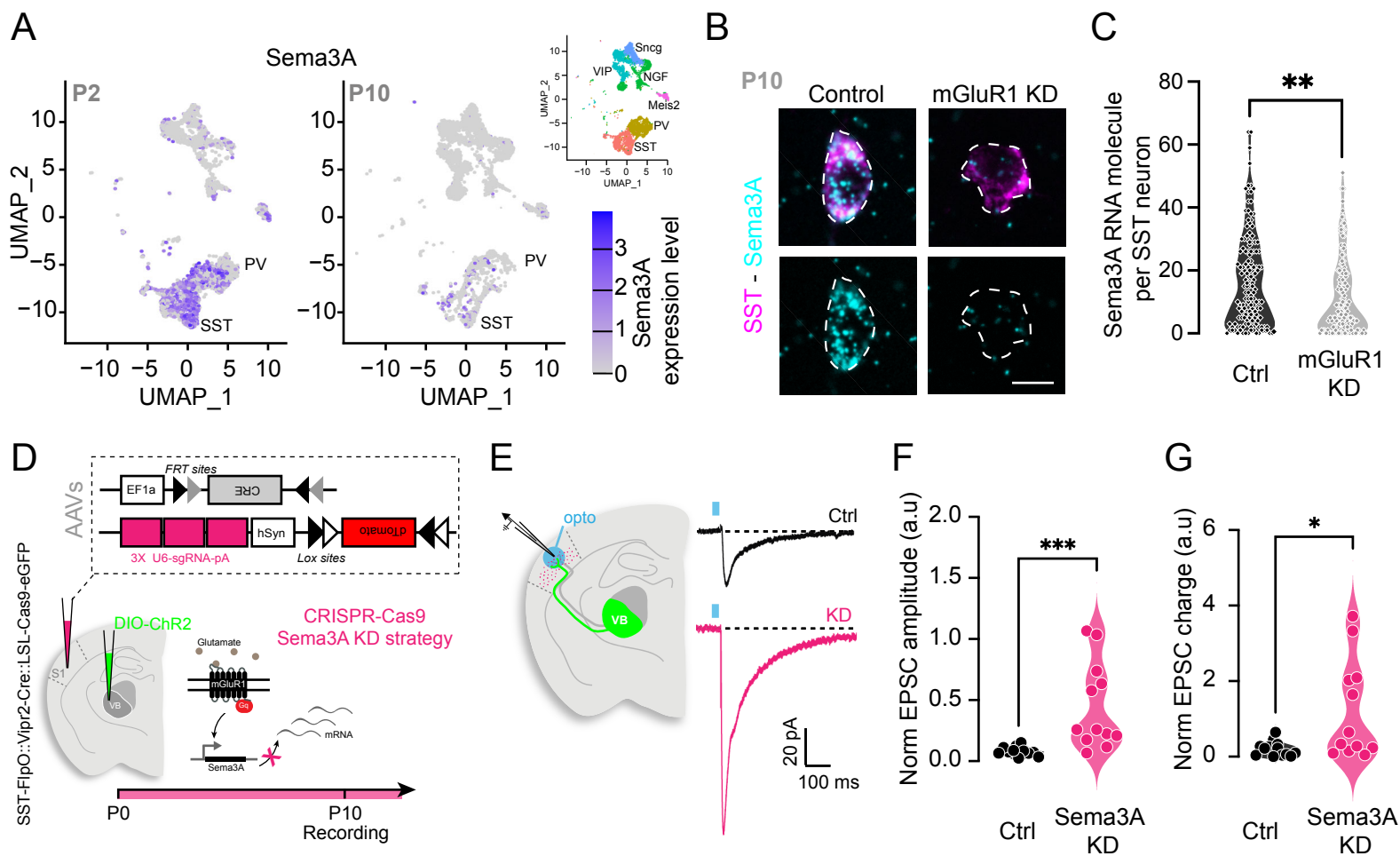
44

Figure 6. mGluR1-dependent Sema3A expression in SST cINs controls their TC transient connectivity

Figure 6: mGluR1-dependent Sema3A expression in SST cINs controls their TC transient connectivity

A) UMAP representation of P2 and P10 scRNAseq with expression levels of Sema3A, showing the high expression in SST cINs at P2. Inset: UMAP representation of integrated P2 and P10 datasets, color coded for the major cIN classes. B) Colocalization of Sema3A labeled using smFISH and SST cINs labeled with Sst immunostaining at P10 in Control and mGluR1 KD. Scale bar: 10 µm. C) Quantification of Sema3A molecule number per SST cIN. The number of Sema3A transcripts is decreased in SST cINs depleted for mGluR1 compared to Control SST cINs. Mann-Whitney test (p-value=0.0041; Ctrl 16.64±1.21 n=148, N=4; mGluR1 KD 12.04±1.05 n=140, N=4). D) Strategy for early deletion of Sema3A in SST cINs specifically, using CRISPR/cas9 system: AAV-driven Flp-dependent Cre expression is driven by SST-FlpO mouse line and controls LSL-Cas9eGFP mouse line. 3x CRISPR single guide RNAs targeting Sema3A are driven by an AAV expressing a Cre-dependent reporter. E) Recording of labeled control and Sema3A CRISPR KD SST cINs upon VB projection stimulation in L5. Example response traces from control SST cINs labeled in response to VB fiber stimulation at P10. F) EPSCs peak amplitudes of SST cINs normalized to the peak amplitude of neighboring pyramidal cells are significantly increased in SST cINs deleted for mGluR1 compared to control cINs at P10. Mann-Whitney test (p-value=0.0001, Ctrl from Fig. 2C 0.08±0.01; Sema3A KD 0.45±0.10 n=12, N=3). G) Normalized EPSC charges of SST cINs deleted for mGluR1 are significantly increased compared to control SST cINs. Mann-Whitney test (p-value=0.0188; Ctrl Fig. 2D 0.20±0.05; Sema3A KD 1.22±0.38 n=12, N=13).
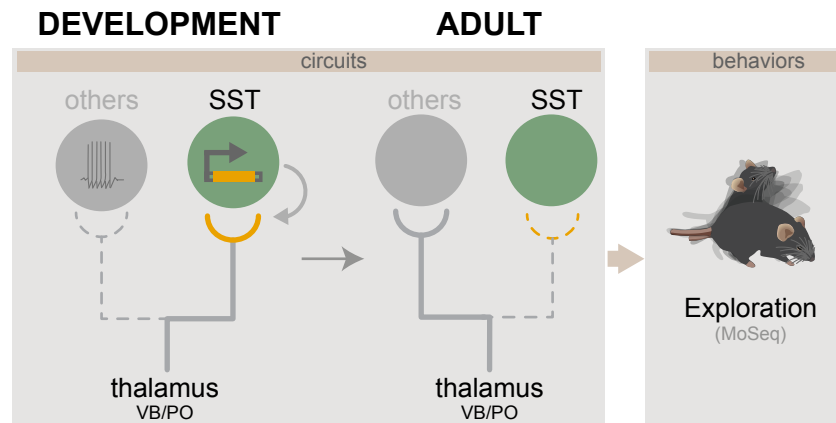
Figure 7. Model for transient TC connectivity development

Figure 7: Model for transient TC connectivity development

In contrast to other neuron types, to which TC connectivity develops according to Hebbian mechanisms, SST cINs receive transient TC inputs from the thalamus. These TC inputs regress onto SST cINs a non-Hebbian mechanism, involving a postsynaptic metabotropic based-transcriptional regulation. This process is required for the maturation of exploratory behaviors in adult mice.